MAGNETIC RESONANCE PULSE SEQUENCES FOR FLUORINE-19

A Thesis

by

ROBIN LYNN TERRY

Submitted to the Office of Graduate and Professional Studies of
Texas A&M University
in partial fulfillment of the requirements for the degree of

MASTER OF SCIENCE

Chair of Committee,	Mark W. Lenox
Co-Chair of Committee,	Mary P. McDougall
Committee Member,	Jim X. Ji
Head of Department,	Gerard L. Coté

August 2014

Major Subject: Biomedical Engineering

ABSTRACT

Cellular therapy is the transplantation of live cells or a cell population in a patient for the treatment of complex diseases. The success of cellular therapy will rely heavily on delivering the cells to their targeted organs or areas of interest. Magnetic resonance imaging (MRI) has the ability to noninvasively track the transplanted cells to ensure they are in the desired destination. Unlike other MRI contrast agents, fluorine-19 has the ability to provide unambiguous cell tracking for two reasons: Fluorinated agents are more readily inert and will not be metabolized quickly so their movement progression can be monitored Additionally, ^{19}F has a limited background MR signal so resulting images will yield positively labeled cells, thus providing successful cell tracking and quantification of cells.

The primary objective of this work was to enable the study of ^{19}F MRI on the Siemens MAGNETOM Verio scanner located at the Texas A&M Institute for Preclinical Studies (TIPS) facility at Texas A&M by making the necessary scanner modifications and pulse sequence adaptions. A $^{19}F/^{1}H$ dual tuned surface coil was purchased from RAPID Biomedical and was used throughout this work. Additionally, pulse sequence modifications to a spin echo sequence and a spoiled gradient echo (called fast low angle shot or FLASH) were made to enable scanning at the fluorine-19 resonant frequency.

A series of experiments were performed with the goal of finding the optimal parameters for each sequence. It was found that the spin density, as compared with the T1 and T2 weighted images, resulted in the highest SNR for the spin echo sequence. The

FLASH sequence with a small flip angle, low TE, and high TR provided the larger signal for the fluorine-19 images. Additionally, a large voxel size for both sequences provided a detectable and quantifiable signal for this type of functional imaging.

T cells were labeled with ^{19}F and imaged to determine sensitivity and labeling efficiency. The goal of this *ex vivo* study was to obtain a reliable and quantifiable signal and image to be the basis for future *in vivo* studies. With the completion of this project, Texas A&M Institute for Preclinical Studies will be equipped with the software and knowledge to perform multinuclear MR imaging, specifically of ^{19}F.

DEDICATION

This thesis is dedicated to my parents for their endless support and love throughout my life. I am deeply thankful for everything they have done for me.

Additionally, I would like to dedicate this thesis to my advisor and mentor, Dr. Mark Lenox. He has never given up on me.

ACKNOWLEDGEMENTS

I would like to thank the many people who have helped me along the way towards obtaining a Master's degree. It is through their advice and assistance that I was able to successfully complete this project.

First and foremost, I would like to thank my advisor and mentor, Dr. Mark Lenox. I am an incredibly lucky graduate student to be able to work with you and all of the unique projects taking place at TIPS. Throughout the years, you have taught me what it means to be a patient scientist and a hardworking engineer. Your positive and caring attitude makes you the best leader I know. Thank you for taking the time to teach me for the past three years.

The imaging lab at Texas A&M Institute for Preclinical Studies has been my second family, and I am very grateful to all of them. Thank you, Maxine Liu for being such a great friend and sister and always offering your help and support. I also want to give thanks to Rachel Johnson who has always been willing to teach me new things about MRI.

I am very grateful to Dr. Colleen O'Connor. You have spent so much of your time growing and preparing the labeled fluorine-19 cells to send to me, and I am truly thankful. You have also been a second advisor to me and offered me guidance when it was much needed. Thank you for everything, including your friendship.

I would also like to thank my committee members, Dr. Mary McDougall and Dr. Jim Ji, for helping me with MRI engineering and for their extreme patience during this

process. Additionally, this work could not have been successful without help from Siemens. Thank you, Dr. Mark Brown, for your valuable class on sequence programming. Dr. David Purdy, thank you for all your advice and help on multinuclear imaging.

Finally, thanks to my family for their never ending support. My grandparents have always pushed me to achieve the most I can, and I am extremely fortunate to have these two wonderful people in my life. My older sister, Kristen, is a great influence and role model for my academics. Alyson, it has been an amazing last year of graduate school living with you, and you have become one of my best friends. My greatest thanks goes to my parents, James and Beth, for always encouraging, loving, listening, and helping me throughout my life. I would not be the person I am today without you two.

NOMENCLATURE

ADC	Analog to Digital Converter
CNR	Contrast to Noise Ratio
FID	Free Induction Decay
FLASH	Fast Low Angle Shot
FOV	Field of View
GRE	Gradient Recalled Echo
ICE	Image Calculation Environment
IDEA	Integrated Development Environment for Applications
MRI	Magnetic Resonance Imaging
MRS	Magnetic Resonance Spectroscopy
NMR	Nuclear Magnetic Resonance
NA	Number of Averages
N_{PE}	Number of Phase Encoding Steps
PFCs	Perfluorocarbons
POET	Protocol Off-line Editing Tool
RF	Radiofrequency
ROI	Region of interest
SDE	Sequence Development Environment
SE	Spin Echo
SNR	Signal to Noise Ratio

SPIOs	Super-paramagnetic Iron Oxide Particles
TA	Acquisition Time
TBW	Time-Bandwidth Product
TR	Repetition Time
TE	Echo Time

TABLE OF CONTENTS

Page

LIST OF FIGURES

Page

LIST OF TABLES

Page

CHAPTER I

INTRODUCTION

Magnetic resonance imaging (MRI) has the unique ability to provide clear *in vivo* images of body organs that would normally be difficult to see through other modalities. MRI emits no ionizing radiation because the energy levels of MRI are on the order of a trillion times smaller than that of x-ray and computed tomography, thus, making MRI an advantageous imaging modality. Additionally, this safely allows scans to be applied repeatedly in order to monitor and track cell movement. The use of multinuclear imaging in MRI has shown great promise in research settings. It allows the ability to target, track, and quantify cells infused with specific compounds that exhibit a net spin. The focus of this work is on fluorine-19.

I.1 Motivation

For many complex diseases, such as an autoimmune or degenerative disease or cancer, cellular therapy is proving to be a potential solution (1-8). Cellular therapy involves transplanting live cells or a cell population into a patient in order to treat diseases (9). The success of cellular therapy will rely heavily on delivering the cells to their targeted organs or areas of interest. The ability to noninvasively track the transplanted cells to ensure they are in the desired destination would be a great benefit to cellular therapy treatments.

Methods, other than MRI, have been used to image cells *in vivo*. Fluorescence and bioluminescence are useful techniques but are limited by their image depth and

resolution (10,11). Positron emission tomography (PET) or single-photon computed tomography (SPECT) are sensitive modalities but are limited by their spatial resolution and involves the use of radioactive materials with a finite half-life (12,13).

MRI has the ability to image and quantify cells *in vivo* in real time. With the help of contrast agents in MRI, researchers are able visualize the labeled cells from the surrounding tissue and monitor their movement. Paul Lauterbur first proved this idea in 1973 when he found that proton imaging of pure H_20 resulted in a different T1 relaxation time than that of H_20 through manganese (Mn) ions (14). Although Mn is not a commonly used MRI contrast agent anymore, other similar T1 contrast agents have been used in MRI for cell tracking. Gadolinium and super-paramagnetic iron oxide particles (SPIOs) are two examples of current contrast agents that affect the MR signal properties of surrounding tissues. Gadolinium must have large amounts of concentration for proper detection (15,16). SPIOs suffer from its disability to accurately discriminate between labeled cells and image artifacts (17-19). These two types of contrast agents could limit the cells' functional parameters while trying to obtain sufficient uptake. Additionally, they suffer from a large proton background signal making cell distinction difficult.

Fluorine-19 MRI has the ability to provide unambiguous cell tracking (20-23). Fluorine has a limited background signal so resulting images will positively yield labeled cells, thus providing successful cell tracking and quantification of cells. Because ^{19}F compounds exhibit their own signal, they can be measured directly. Unlike SPIO, fluorinated agents are more readily inert and will not be metabolized quickly so their movement progression can be monitored, as well (20-23).

Scanner hardware and software modifications are required in order to run a sequence at the ^{19}F resonant frequency. This work describes the process of the enabling the study of fluorine-19 cell tracking at Texas A&M Institute for Preclinical Studies (TIPS) through testing of multinuclear MRI pulse sequences.

I.2 Thesis Chapters and Organization

The main content of this thesis is divided into three specific aims:

Specific Aim 1: Test a multinuclear spin echo pulse sequence.

Specific Aim 2: Test a multinuclear fast low angle shot (FLASH) pulse sequence.

Specific Aim 3: Acquire *ex vivo* images.

A general background will be used to describe the physics of MRI in Chapter II, followed by the potential use and importance of fluorine-19 in MRI in Chapter III. The details and approach of creating the multinuclear compatible spin echo sequence will be delivered in Chapter IV. Chapter V will include an in-depth approach to creating Siemen's FLASH multinuclear sequence. Both Chapters IV and V will include an explanation on the RF pulses, applicable gradients, resulting echoes, and multinuclear conversions. These sequences will be tested on a 3T MRI scanner using different concentrations of fluorine-19 phantoms and ^{19}F labeled cells. Finally, in Chapter VII, conclusions to this work and the importance of multinuclear will be readdressed, along with the goals and plans for potential future work.

CHAPTER II

BACKGROUND

In 1946, Felix Bloch and Edward Purcell independently described the magnetic properties of certain nuclei, a physiochemical phenomenon known as nuclear magnetic resonance, NMR (24,25). This development furthered and introduced magnetic resonance spectroscopy (MRS), a method to study metabolic changes and tissue characterization. In 1973, Paul Lauterbur changed the course of imaging when he first introduced the idea of using magnetic field gradients and a backprojection technique to produce two-dimensional images of the body (14). In 2003, Lauterbur and Peter Mansfield, for his work in mathematically analyzing signals and obtaining fast imaging, received the Nobel Prize. With these, and many other contributions, MRI has become a powerful diagnostic tool, and as the field of MRI continues to grow, so do the opportunities.

II.1 MRI Physics

II.1.1 Magnetic Spin

Any electric charge, whether it is positive or negative, produces a magnetic field. Although a proton is not large in size, it spins very fast and, such, is able to produce a noticeable magnetic field. When in the vicinity of a large external magnetic field, B_0, most of the small spinning protons align parallel with the external field (Fig. 1).

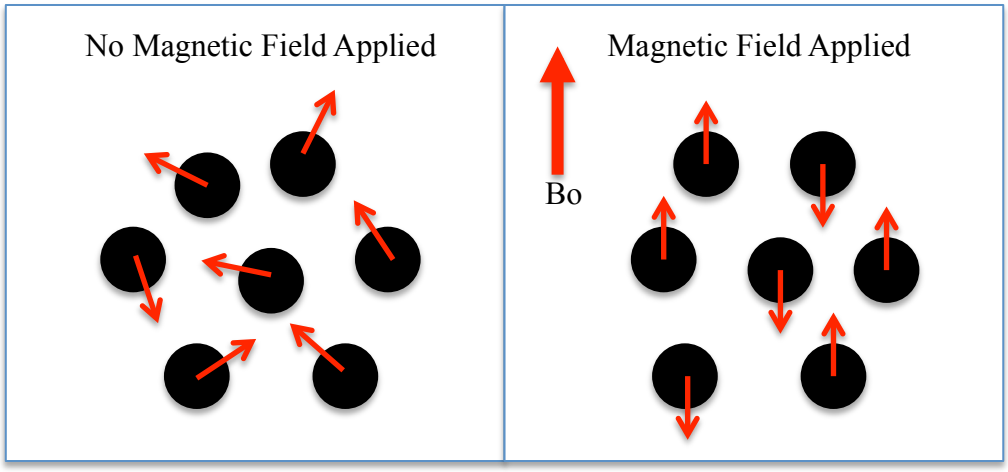

Figure 1: Polarization of spins. No magnetic field applied shows spins are randomly oriented. When located in an external magnetic field, the spins align in the direction of the magnetic field resulting in a net magnetization.

Protons precess about the axis of the external magnetic field. The Larmor equation,

$$\omega = \gamma B_0 \quad (1)$$

shows the direct proportion between the frequency of the precession and the strength of the magnetic field, where ω is the Larmor frequency and γ is the gyromagnetic ratio. The gyromagnetic ratio is unique for each nucleus that has a magnetic moment.

The common MRI orientation considers longitudinal magnetization, M_z, the magnetic moment vector in the z direction, while the transverse magnetization, M_{xy}, is the vector component in the x-y plane, the direction perpendicular to the z-axis (Fig. 2).

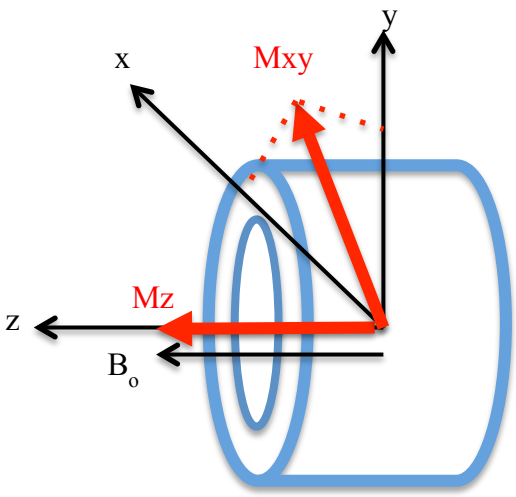

Figure 2: MRI orientation showing x, y, and z directions from scanner isocenter. M_{xy} refers to the transverse magnetization and M_z refers to the longitudinal magnetization, which is in the same direction as the external magnetic field.

II.1.2 Excitation and Relaxation

When an electromagnetic radiofrequency (RF) pulse is applied at the Larmor frequency, the proton can absorb that energy and change alignment. This is described by the tip angle, α, which is the angle between the tipped magnetization and the longitudinal axis. It depends on the strength and duration of the RF pulse. This generates a strong, measurable signal. However, this is a high-energy state, and the protons will not stay in this unison precession forever. Once this RF pulse is turned off, the absorbed RF energy is retransmitted at the resonant frequency and generates an NMR signal called a free induction decay, or FID. Quickly, the precessing protons relax and release their excess energy.

A process called T1 relaxation occurs when the excited spins in the longitudinal magnetization align to the original orientation in line with the magnetic field. Simultaneously, there is dephasing in the transverse direction. Because the protons precess at individual speeds, the signal degenerates as the protons precess out of phase with each other, an event known as T2 or spin-spin relaxation (Fig. 3). The signal loss associated with the dephasing of each magnetization is called T2* relaxation.

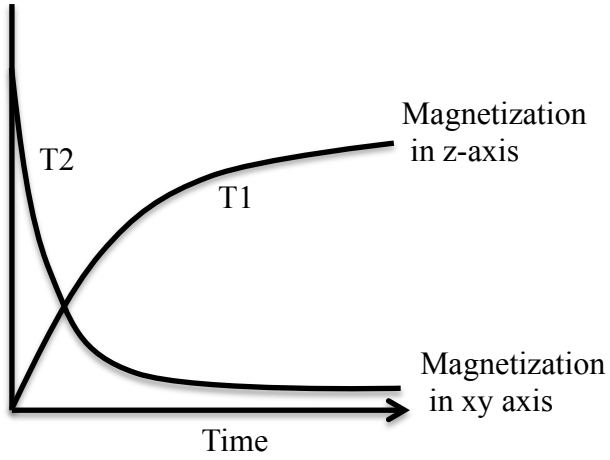

Figure 3: Relaxation rates for T1 recovery and T2 decay.

II.1.3 Gradients and Image Formation

In order to create an image, gradient coils are used to resolve spatial position. There are three gradients, G_x, G_y, and G_z, generated by separate gradient coils located inside the scanner and provide a linear variation in the magnetic field in the longitudinal direction:

$$B = (B_0 + G_x x + G_y y + G_z z)\, z \quad (2)$$

Each coil has its own inductance, resistance, and amplifier thus making them independent of each other. These gradients include the slice select, phase encoding, and frequency encoding (or readout) gradients. The slice selection gradient chooses the section, or slice, to be imaged. The phase encoding gradient allow for localization of the signal by its phase due to a phase shift in the signal. Finally, the frequency encoding allows for position to be determined by frequency due to a frequency shift in the signal. With the combination of these gradients and their corresponding changes in field strength, the resonant frequency also changes thus making the received signal dependent on position.

The resulting signals containing the raw data matrix are stored in Fourier space, or k-space. Once an RF excitation pulse and slice select gradient are applied, the sequence begins. If there is no phase encoding or readout dephasing turned on, then the center of k-space will be filled. This will contain the strongest signal because there is no dephasing due to phase encoding gradients taking place. The central lines of k-space contribute to signal and contrast. The other k-space lines will continue to fill according to the polarity of the phase encoding gradient (denoted as G_{PE} in Fig. 4 and G_y in Eq. 3) and frequency encoding gradients (denoted as G_{FE} in Fig. 4 and G_x in Eq. 3). The outer lines of k-space relate to the resolution of an image. The amplitude of the phase encoding gradient will determine how far up and down a line of k-space is filled. Similarly, the amplitude of the frequency encoding gradient will determine how far to the left and right k-space is filled. For example, a negative phase encoding gradient and a

negative dephasing frequency encoding gradient will start to fill the k-space line at the bottom left (Fig. 4). Then the second frequency encoding gradient, the positive one, will fill the line of k-space going from the left to the right until that row is complete. Typical spin echo and gradient echo sequences follow this rectilinear data acquisition method.

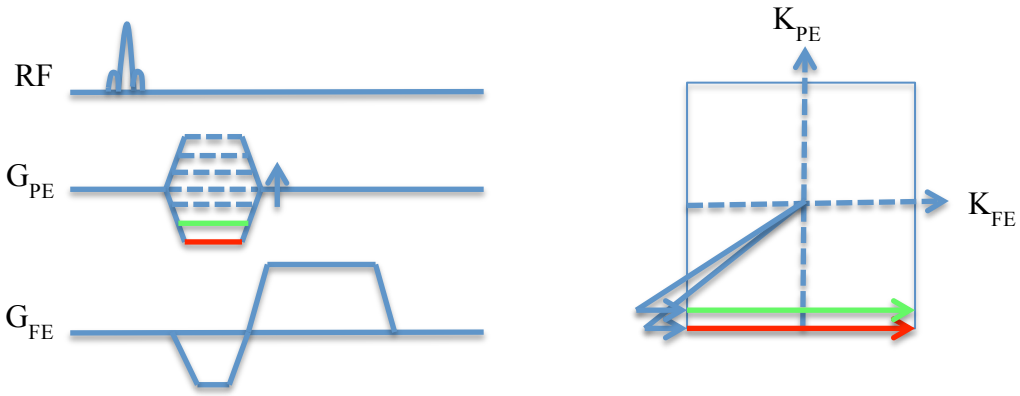

Figure 4: A simple gradient echo with its resulting k-space. The red line at the bottom of the phase encoding gradient corresponds to the red line at the bottom of k-space. Next, the green line from the phase encoding gradient fills the green line of the k-space.

A fundamental topic in MRI is the reconstruction process. It can be shown that an MR image is reconstructed as the inverse 2-D Fourier transform. A baseband MR signal can be written as:

$$S(t) = \iint_{object} \rho(x,y)\, e^{i\gamma G_x x t + i\gamma G_y y \tau}\, dxdy \qquad (3)$$

where $\rho(x,y)$ is the image and τ is the time during phase encoding activation. Furthermore, because the integral is only over spatial dimensions, k-space can be defined as:

$$k_x = (-\gamma G_x t) \text{ and } k_y = (-\gamma G_y \tau) \tag{4}$$

This reduces the integral to:

$$S(k_x, k_y) = \iint_{object} \rho(x, y)\, e^{-i k_x x - i k_y y}\, dxdy \tag{5}$$

This equation now resembles the 2-D Fourier integral. To solve for $\rho(x,y)$, an inverse Fourier transform is taken:

$$\rho(x,y) = FT^{-1}[S(k_x, k_y)] = \iint_{k-space} S(k_x, k_y)\, e^{i k_x x + i k_y y}\, dk_x\, dk_y \tag{6}$$

This shows that k-space is the Fourier transform of the image. The equations above were derived from (26).

II.2 Multinuclear MRI

Hydrogen is the most frequently imaged nucleus in MRI because of its large abundance in biological tissues. Typically, this conventional imaging has high SNR due to the protons' high natural and biological abundance and high gyromagnetic ratio. Hydrogen has gyromagnetic ratio of 42.58 and is the main nucleus used in MRI because it is the simplest atom in the periodic table containing only one proton. Additonally, it has a magnetic moment.

Since some of the first experiments by Paul Lauterbur, MRI has become more advanced, thus, leading to the idea of multinuclear imaging. Any nucleus with a net nuclear spin, meaning it has an odd atomic number or weight, has the potential to be imaged in MRI. A nucleus exhibits a net nuclear spin if it has an odd atomic number or

weight. Therefore other nuclei, not just hydrogen, can be used with the correct adjustments in MRI. For example, some common nuclei used for MRI imaging include helium-3, lithium-7, carbon-13, fluorine-19, sodium-23, phosphorus-31, and xenon-129. While multinuclear is commonly not used in a clinical setting, it has shown great promise in a vast number of studies (27-33).

II.3 Pulse Sequencing

MRI has the ability to change the way a tissue is imaged by manipulating the generated magnetic fields. The method by which these fields can change is known as a pulse sequence. An MRI pulse sequence has a designated number of RF and gradient pulses that produce the data to form the image.

II.3.1 Siemens Pulse Sequence Development

Numaris 4, or syngoMR, is the Siemens software used on all MR products. It gives users the ability to quickly create and edit pulse sequences using the common C++ language. The interface in which to program sequences is called IDEA, or Integrated Development Environment for Applications. IDEA consists of two parts: Software Development Environment (SDE) and Image Calculation Environment (ICE). SDE is the environment that allows user complete freedom to create pulse sequences while ICE is involved with data acquisition and image calculation and reconstruction. This research will involve SDE, not ICE.

The pulse sequence construction is compiled on a stand-alone computer that is a Windows XP operating system with Microsoft Visual Studio 6.0 installed for the C++ programming. Once the sequence is compiled, a sequence unit test, developed by

Siemens, will check to make sure the sequence does not fail any hard limits required on the type of scanner selected. Additionally, it will check timing, image orientation, and other aspects. Another method to check for sequence errors is in the protocol off-line editing tool (POET). POET allows user to interface with the protocol by changing different parameters and displaying its resulting graphical pulse sequence. After making modifications to a sequence, the unit test and POET must pass successfully before transferring the necessary compiled files to the scanner for execution.

This research focuses on adapting multinuclear capabilities for two different pulse sequences: a spin echo and a spoiled gradient echo called a FLASH (which stands for Fast Low Angle Shot).

CHAPTER III

FLUORINE-19

MRI using ^{19}F presents opportunities for labeling cells and monitoring cell movement.

III.1 General Properties

Fluorine-19 is the only stable fluorine isotope. It has a nuclear spin of ½ and a high gyromagnetic ratio of 40.05 MHz/T, that is 94% of that of ^{1}H. It exhibits short spin-spin or T2-relaxation times, thus benefiting from a low background signal. This gives ^{19}F the ability to have an exceptionally high contrast-to-noise ratio especially when a fluorine agent is used. This fluorine agent should have a large ^{19}F nuclei density on the molecule and a high tissue concentration in the hopes of having a resulting image comparable to that of proton images (34).

III.2 Perfluorocarbons

Perfluorocarbons (PFCs) are the molecule of choice in this study because they are able to achieve the desired signal and image results due to their sizable density of ^{19}F nuclei. Perfluorocarbons are a class of molecules similar to hydrocarbons except the hydrogen atoms are replaced with fluorine atoms. This carbon-fluorine bond is considered the strongest single bond in organic chemistry making PFCs a strong and stable compound (35). They are highly hydrophobic and somewhat lipophobic giving them the ability to affect some cellular responses. PFCs have a low water solubility meaning they diffuse slowly and will stay at the target site for an extended period. Due

to its low Van der Waals forces, PFCs have low intermolecular adhesion, high vapor pressure, and low surface tension. This can be advantageous as it allows the molecules to encase and cover a potential tumor, which can help prevent the tumor's growth.

PFCs have no known enzymes that can metabolize it, they do not degrade at typical lysosomal pH values, and the chemical shift is not altered when injected inside cells; therefore, it is a consistent tool to use for *in vivo* studies. The ^{19}F MRI detects the density of the ^{19}F spins (or nuclei) contained in the PFC droplets. Because this concentration is typically low, the signal-to-noise ratio will be lower than the common ^{1}H images. Fortunately, there is no ^{19}F background, so the generated signal is coming directly from the labeled cells.

III.2.1 Perfluorocarbons in MRI

The first *in vitro* ^{19}F images date back to 1977, which introduce the use of ^{19}F molecules, such as PFC, as tracers. Around this time, PFCs were studied further on their biological properties, one of which was their high oxygen affinity. In 1966, a study conducted by Clark and Gollan demonstrated that mice submerged in fluorocarbon liquid saturated with oxygen could survive for extended periods of time (36). This showed the value of PFCs as a potential method to increase tissue oxygenation thereby making forms of radiation treatment a more sensitive approach.

In 2008, PFCs were used to label macrophages in the infarcted myocardium of mice subjects thus showing that PFCs could be used as a contrast agent for inflammatory responses (22). Labeling and tracking of immune cells was furthered observed and compared against other methods such as PET and SPECT (20). The MRI images of the

labeled cells can be imposed with the anatomical ^{1}H images, therefore, giving MRI a clear advantage over other hazardous modalities.

III.3 Fluorine-19 Coil

RAPID Biomedical manufactured the $^{19}F/^{1}H$ flexible surface coil. Typically, surface coil allows a higher localized SNR as compared to a volume coil but has a low depth penetration (37,38). The higher SNR can be beneficial in multinuclear studies because signal acquisition can be difficult. This is a transmit- receive coil and has an interface box, which allows the coil to connect to the Siemens Verio through transmit and receive ports on the bed (Fig. 5).

Figure 5: RAPID Biomedical coil set-up showing flex coil inserts into interface box, which plugs into sockets 1 and 4 on the MRI scanner bed.

It has linear polarization and a fixed resonant frequency for ^{1}H and ^{19}F at 123.2 MHz and 115.9 MHz, respectively. The coil configuration is made up of a circular ^{19}F coil enclosed around a butterfly hydrogen coil (Fig. 6). This means the SNR will be greatest at the center of the coil (39,40).

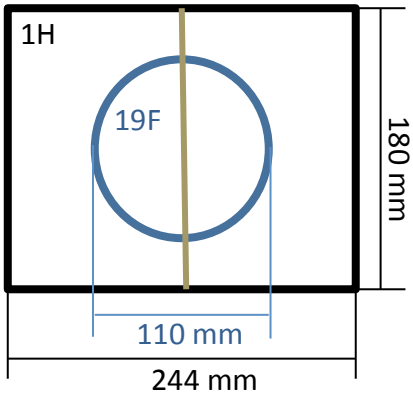

Figure 6: RAPID Biomedical coil configuration with fluorine-19 coil enclosed within a hydrogen coil.

III.4 Cell Sense

Celsense, Inc. is a company located in Pittsburgh, PA that makes fluorine-19 products for researchers to test inflammation and cellular therapeutics using MRI.

III.4.1 Phantoms

For optimizing scanning parameters, a ^{19}F MRI phantom set developed by Celsense was used. This phantom set contains their product, Cell Sense, which is a PFC-based emulsion designed to label cells and track their migration using ^{19}F magnetic

resonance imaging or spectroscopy. The phantoms are a color-coded dilution series in a semi-solid medium sealed by epoxy, as shown in Fig. 7. Each vial contains a differing amount of fluorine-19.

Figure 7: Cell Sense 10 mL phantoms in decreasing fluorine-19 strength from top to bottom.

The largest amount to smallest amount of concentration is: yellow, red, green, and then blue. Table 1 shows the concentration strength and the amount of ^{19}F spins/mL.

Table 1: Cell sense phantom set

Color	19F:1H Ratio	19F Concentration (spins/mL)
Yellow	1:5	$4.1x10^{18}$
Red	1:15	$1.3x10^{18}$
Green	1:45	$5.8x10^{17}$
Blue	1:135	$2.3x10^{17}$

III.4.2 *Ex vivo* Labeling

In this research, we tested the labeling of dog T cells with a commercially available ^{19}F contrast agent developed from Celsense, Inc. This ^{19}F agent, a type of Cell Sense called CS-ATM-1000, is a PFC-based emulsion designed to label cells and track their migration in animal studies using ^{19}F magnetic resonance imaging or spectroscopy. The process of growing the cells and labeling them with CS-ATM-1000 is further described in Chapter VI.

CHAPTER IV

MULTINUCLEAR SPIN ECHO

The spin echo (SE) sequence is the most commonly used pulse sequence. The spin echo is made up of a slice selective 90° (or excitation) pulse, one or more 180° rephrasing pulse, and the resulting signal. The two main variables in a spin echo sequence are the repetition time (TR) and the echo time (TE) and changing these values will change the contrast weighting of the image. TR represents the time between consecutive 90° pulses, and TE represents the time between the midpoint of the application of the 90° pulse and the peak of the echo signal (Fig. 8). The TR and TE values can be adjusted to give a T1-weighted, proton or spin density, and T2-weighted images.

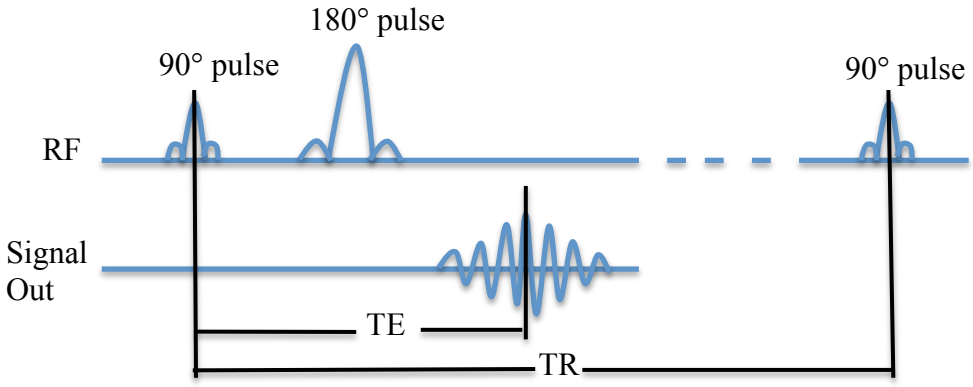

Figure 8: Spin echo sequence showing TE as the time from the middle of the RF pulse to the middle of the echo and TR as the time between consecutive RF pulses.

The advantages of using SE sequences are resulting images with high SNR and minimal susceptibility effects. However, with this come longer scan times and more required RF power (41). For instance, the acquisition time (TA) for the SE is given by:

$$TA = TR * N_{PE} * NA \quad (7)$$

where N_{PE} is the number of phase encoding steps and NA is the number of averages.

The main set up for the SE sequence has two RF pulses, gradient pulses in the x-, y-, and z-direction, and an ADC signal detection readout.

IV.1 Radiofrequency Pulses

The RF pulses are a time varying amplitude, which excite only a certain band of frequencies on either side of the Larmor frequency. The range of the frequencies depends on the length of the RF pulse and the slice thickness selected. It is only these excited frequencies that will contribute to the signal of the spin echo.

The first RF pulse, the excitation, has duration of 2048 microseconds; the second RF pulse, the refocusing, is twenty percent larger than the excitation pulse with duration of 2560 microseconds. Additionally, the ratio of the refocusing pulse and the excitation pulse must be approximately greater than 1.2 due to the scanner's hardware limits. As shown, the excitation pulse spectrum (Fig. 9a) was more precise than the refocusing pulse (Fig. 9b) due to the high power requirements for the refocusing pulse, roughly four times as high. This pulse is made wider than the refocusing pulse in order to still envelope the excited slice.

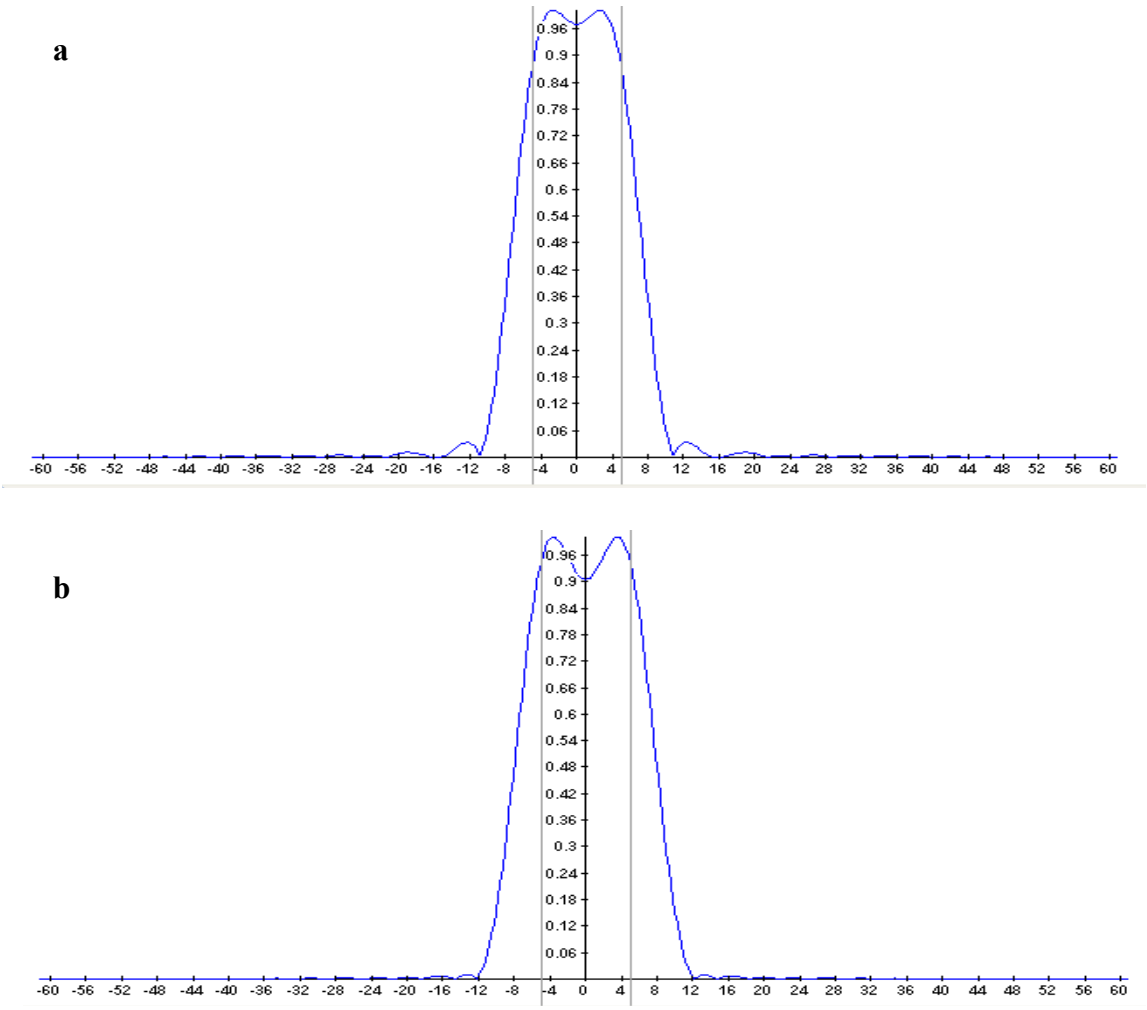

Figure 9: RF pulse shape used in Siemens spin echo. a) Normalized absolute part of the time domain for the RF excitation pulse. b) Normalized absolute part of the time domain for the RF refocusing pulse.

IV.2 Gradients

The gradient fields' role is to spatially encode information in order to form an image in the reconstruction phase. In addition to the main gradients used in a spin echo, this sequence incorporates spoiler gradients, which kills the unwanted MR signals that

could produce image artifacts. The gradients are all trapezoidal shaped with the terminology shown (Fig. 10).

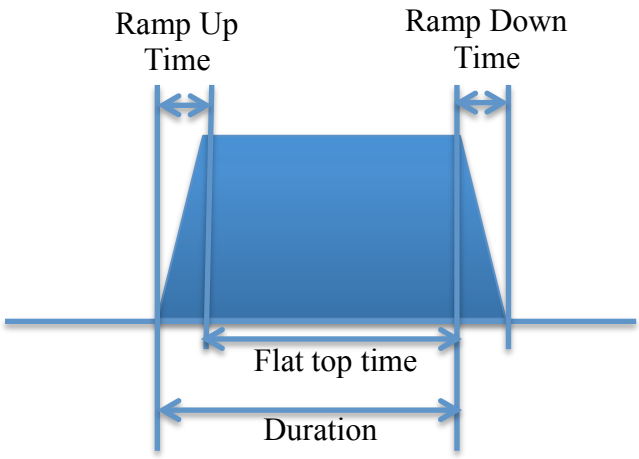

Figure 10: Trapezoidal gradient showing the ramp up and down times, flat top time, and duration.

When referring to gradient duration, this time is the ramp up time plus the flat top time. Due to scanner qualifications, the gradient timings, including ramp times, must be a multiple of 10 microseconds.

IV.2.1 Slice Select

There are three slice select gradients: slice excitation gradient, slice rephrasing gradient, and slice refocusing gradient. Each gradient will have the necessary amplitude to achieve the requested slice thickness given the bandwidth of the RF pulse. Furthermore, the RF pulse will know the appropriate slice thickness and can therefore

calculate the gradient amplitude. The advantage of this is if the RF pulse needs to be changed, then the sequence will adjust the flat top times and gradient amplitudes, as well. The mathematics of the relationship can be shown below:

$$G_{SS} = \frac{2\,\pi\,\Delta f}{ST} \tag{8}$$

where G_{SS} is the magnitude of the slice select gradient, ST is slice thickness, and Δf is the RF pulse bandwidth of frequencies. Therefore, if the slice thickness is decreased, then the slice select amplitude will increase for a constant RF bandwidth.

The amplitude of the slice refocusing gradient is roughly 80% of the slice excitation gradient in order to avoid parasitic excitation or "third arm" artifact, where spins are excited that are outside the region of interest. The area of the slice rephasing gradient will be equal to the area of the slice excitation gradient starting at TE=0 (or the middle of the excitation RF pulse) to the end (Fig. 11).

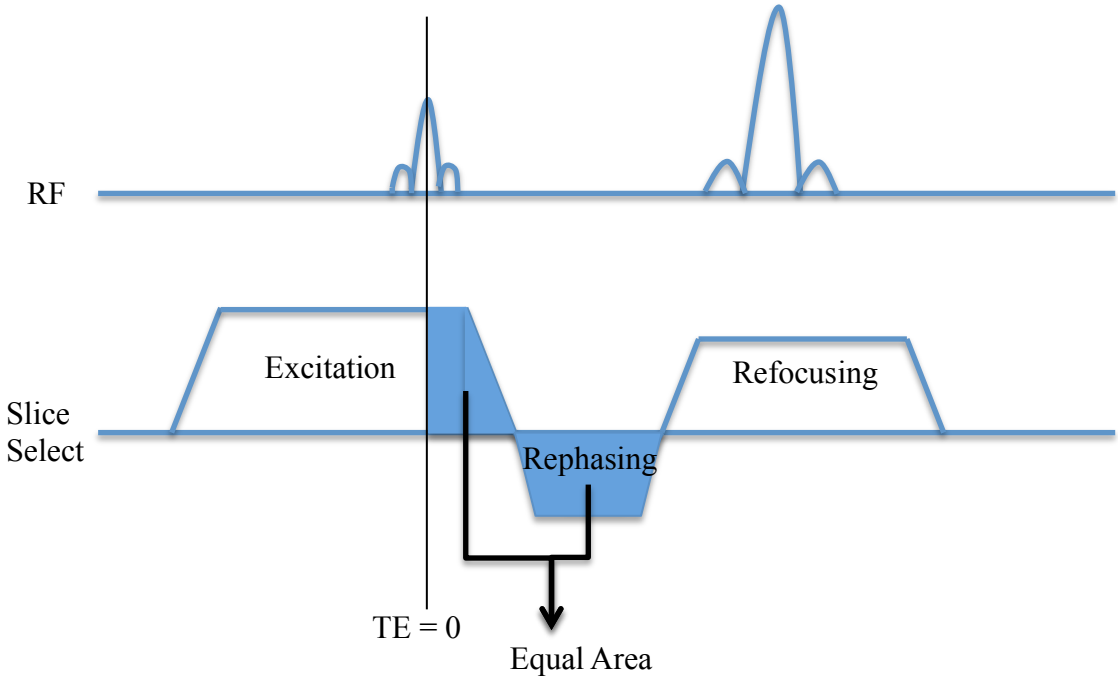

Figure 11: Slice select gradient for spin echo sequence.

The slice rephasing gradient has negative polarity in order to compensate for the phase dispersion leading to signal loss caused by the slice select gradients.

IV.2.2 Phase Encoding

In the phase encoding direction, the two gradients used are the spoiler gradient and the table gradient. The table gradient occurs in between the two RF pulses, and the spoiler gradient occurs at the end of each TR cycle (Fig. 12). Its purpose is to vary the phase of the transverse magnetization. This table gradient is repeated until all of the phase encoding steps has been recorded into k-space. In addition, the duration is kept as short as possible (in this case it is less than 4 milliseconds) in order to minimize TR, if wanting to acquire T1 weighted images.

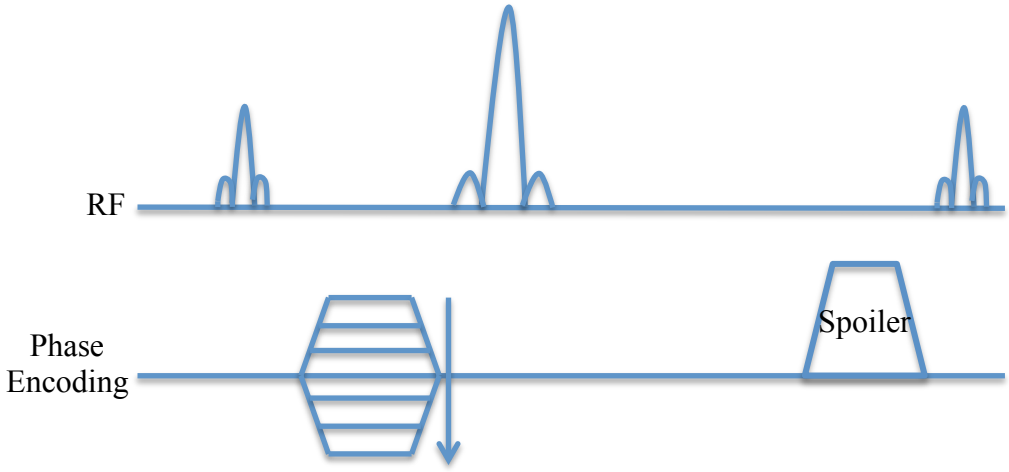

Figure 12: Phase encoding gradient for spin echo sequence with additional spoiler gradient at end of TR cycle.

The role of the spoiler gradient is to dephase the transverse magnetization along the direction of the gradient while leaving the longitudinal magnetization preserved. Therefore, this gradient is able to kill the unwanted MR signals that would produce image artifacts.

IV.2.3 Readout

The frequency encoding direction contains the readout and its accompanying dephasing gradient. The purpose of the readout gradient is to spatially encode the tissue along the direction of the gradient. For this spin echo sequence, these are the readout spoiler gradient, the readout dephasing gradient, and the readout gradient pulse (Fig. 13).

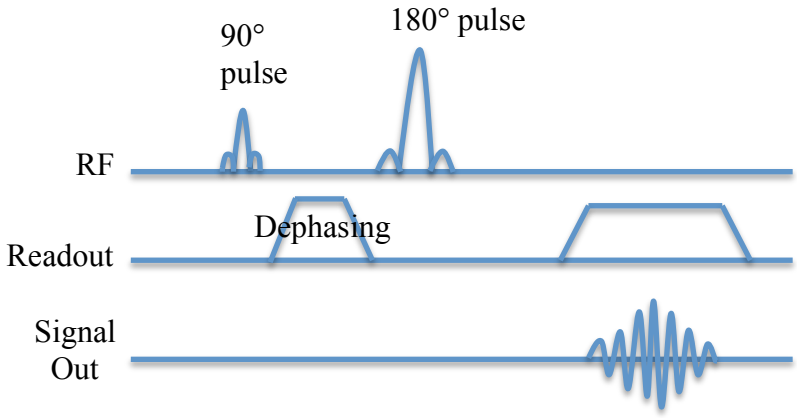

Figure 13: Frequency encoding direction for spin echo showing dephasing and readout gradient.

The refocusing RF pulse separates the dephasing gradient and readout gradient. This provides the spin echo with having a shorter minimum TE, which aids in creating a T1 weighted image or spin density image. These gradients, also, have a positive polarity due to the RF refocusing pulse negating the phase of the dephasing gradient. The readout gradient is left on throughout the formation and dissipation of the echo. The dephasing gradient prepares the transverse magnetization in order to later create an echo.

IV.3 ADC Object

During the time the readout gradient is on, the RF coil receives the spin echo RF signal. To do this, the analog-to-digital converter (ADC) detects the small current induced in the RF coil by the formation of the spin-echo, samples the analog MRI signal and converts it to digital format, as the name ADC suggests.

The columns, dwell time, and bandwidth define the ADC object. The columns are defined by the base resolution defined by the user. The dwell time is the time

between successive sampling points and is calculated by the inverse of the Nyquist frequency for an image field of view (FOV) or in terms of duration and base resolution:

$$\text{Dwell Time} = \frac{\text{ADC}_{\text{DUR}}}{\text{Base Resolution}} \tag{9}$$

This means the dwell time (or the time between sampling points) multiplied by the number of columns (or the base resolution of the image) is equal to the ADC object duration (Fig. 14).

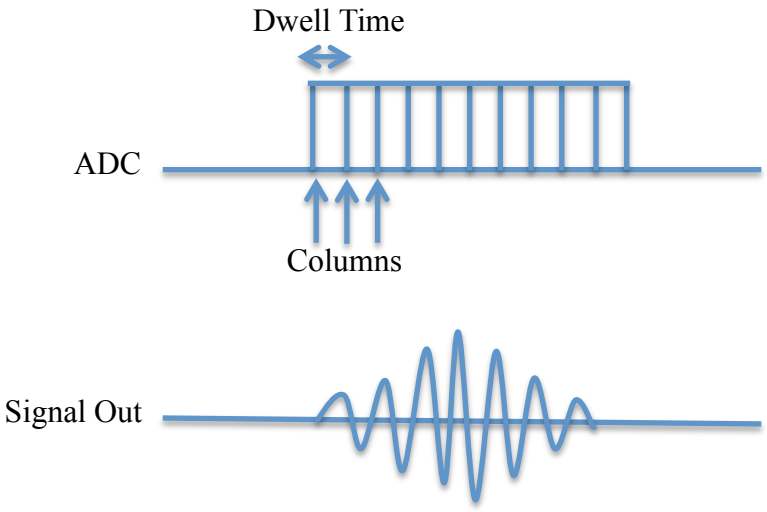

Figure 14: ADC showing dwell time is time between each column, or sample.

The default bandwidth of the ADC object is 130 Hz/pixel and can be changed in the sequence program accordingly.

IV.4 Multinuclear Option and Other Parameters

In order for multinuclear imaging, the scanner and sequence must have the capabilities for this. The scanner must be multinuclear compatible, meaning that it is able to recognize nuclei other than hydrogen. Additionally, the sequence must be edited with the multinuclear option active. It is possible to make one sequence compatible with all available nuclei or make one sequence focus primarily on the nuclei of choice. The sequence created in this thesis is only applicable to fluorine-19, not the other nuclei. This is because 19F has a higher gyromagnetic ratio (only 6% different than that of hydrogen) compared to other nuclei so some changes were not applicable here. For nuclei with lower gyromagnetic ratio, higher gradient strengths would be needed.

Another multinuclear addition to be made is adding two libraries to the SE makefiles. Makefiles are required files when programming in SDE and contain the libraries the C++ code plans to access. Therefore, in order for the C++ code to recognize the change of nucleus from ^{1}H to ^{19}F, its makefiles must contain the necessary libraries. These libraries contain important information, such as the gyromagnetic ratio, on the other nuclei, and are called “MeasNucleiBase” and “MeasNucleiIF”. If these libraries are not added, errors will occur when trying to resonant at a frequency other than that of hydrogen.

Additionally, for each new coil made that is not supplied from Siemens, new coil and plug files are required. These software files allow the communication between the scanner and the coil. The coil used in this research was purchased from RAPID

Biomedical (as described in Chapter III); therefore, they supplied the necessary coil and plug files. These files were installed in the scanner computer.

The parameters described below are user controlled in the User Interface design, assuming the parameters do not break the scanners hard limits. The number of slices, TR, and TE are user controlled, but also dependent on other parameters. A rough approximation of this relationship for a simple spin echo is:

$$\text{Maximum number of slices} < \frac{\text{TR}}{\text{TE}} \tag{10}$$

Unlike CT, the number of slices does not directly affect the overall scan time in MRI. However, if TR is decreased (which decreases scan time), then the number of available slices decreases.

For this sequence, the slice thickness has a minimum and maximum of 2 mm and 10 mm, respectively. However, as before, these available thresholds can change depending on two parameters: changing the slope of the slice selection gradient and changing the bandwidth of the RF excitation pulse.

IV.5 Virtual Simulation

After successful compilation of the multinuclear pulse sequence C++ code and its necessary make files, a unit test was performed to test various parameters and sequence timings. The unit test was successful (Fig. 15) and displayed as an HTML file. The coil and plug files from RAPID Biomedical were copied to the customer coil file section in IDEA.

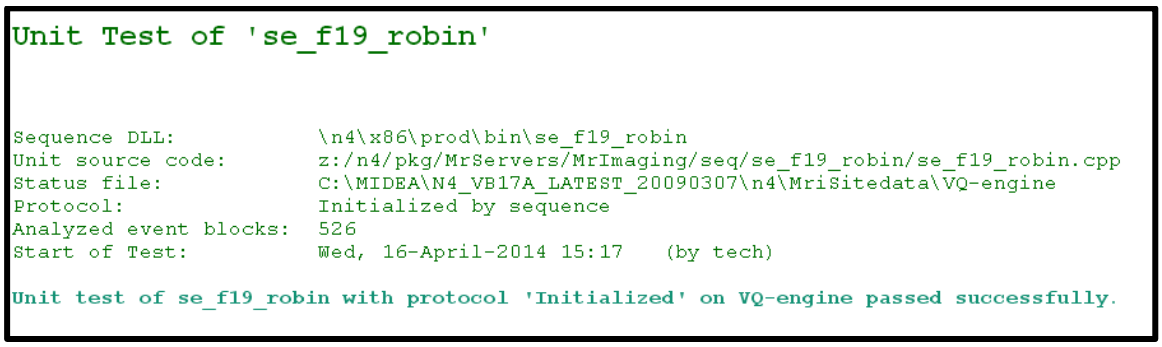

Figure 15: Successful unit test of fluorine-19 spin echo.

Then the virtual coils were edited to select for the 19F/1H surface flex coil, as shown in Fig. 16. In order to do this, the coil files provided by RAPID Biomedical were examined to verify they had the correct code that allows them to communicate with the IDEA interface. If they were lacking this, it would need to be added in order to use this coil in the virtual system inside POET, and the coil files would have to be recompiled to receive a new CheckSum through the scanner computer. Once it was verified the coils contained the necessary information, they were then copied into their appropriate file destination made for customer created coil and plug files within IDEA. In the SDE command box, code was written to enable this conversion from Siemens created coil and plug files to those created by customers. For this particular coil, since it plugs into sockets 1 and 4 on the MRI bed, the plug files were activated for those ports. Sockets 1 and 4 represent transmit and receive ports, respectively. The remaining 8 sockets were activated by the MRI's build in body coil as default. The virtual coils were selected inside POET, which aid in testing the multinuclear sequence before using it directly on the scanner.

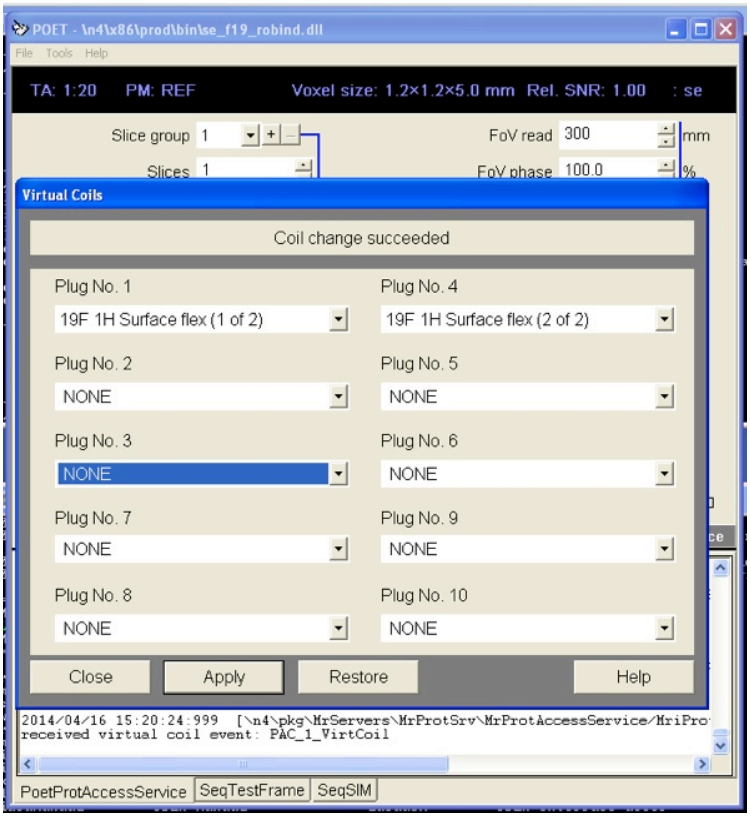

Figure 16: Virtual coil file change success.

A graphical pulse sequence in POET was obtained to make sure the RF pulse, the gradients, and ADC were positioned and calculated correctly (Fig. 17). The parameters used for this simulation was 10 slices at 20% distance factor with transversal orientation, voxel size of 3.9x3.9x5.0 mm^3 with TR of 650 ms and TE of 15 ms. A small TR was chosen for simplicity and speed.

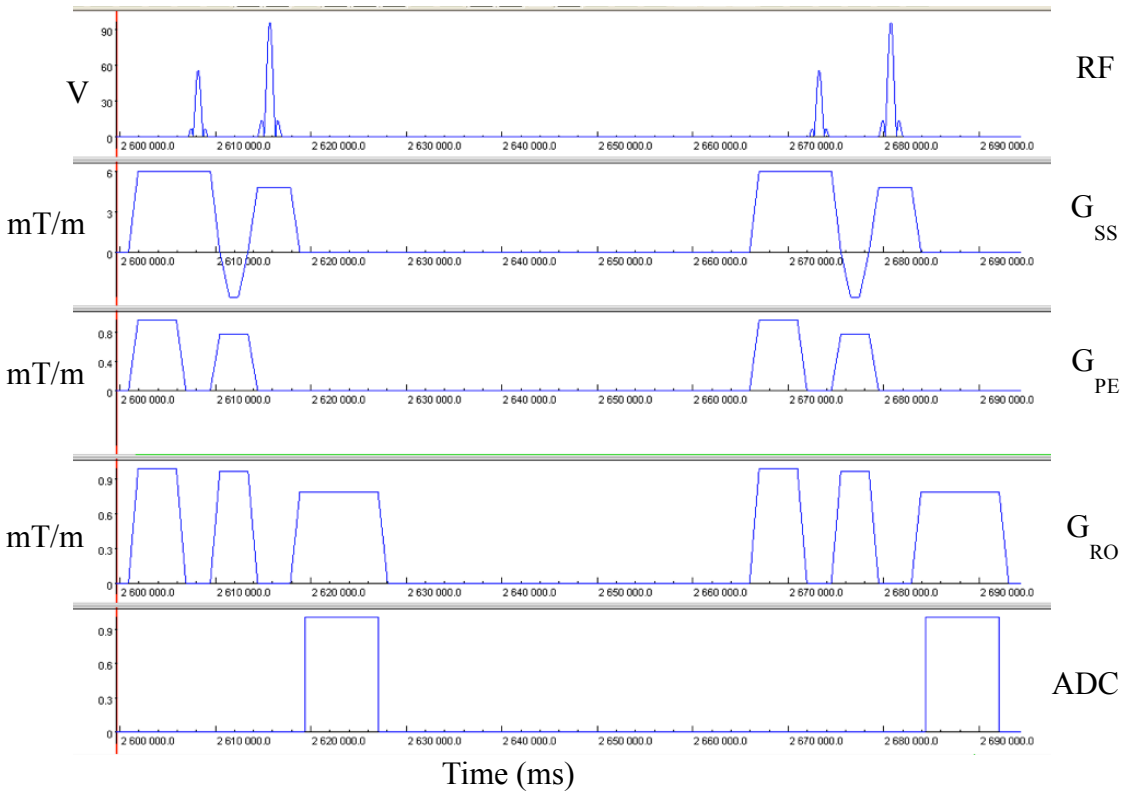

Figure 17: Virtual simulation of spin echo.

The virtual simulation shows two complete rounds of each RF set. As stated earlier, the amplitude of the RF pulse depends on factors such as slice thickness and gradient amplitude. This is given in units of volts. Each gradient has units of mT/m while the ADC is unitless and will either have a value of 0 or 1. It should be noted that the spoiler gradients in the phase encoding and readout directions appear to be occurring at the beginning of each sequence but are actually occurring at the end of the previous TR cycle.

IV.6 Cell Sense Phantom Imaging

To get a basis for signal detection for *ex vivo* cells and future preclinical studies, phantoms containing different ^{19}F concentrations were scanned. The phantoms were created by Cell Sense, Inc. and are a fluorocarbon-based emulsion. Different sequence parameters were used for comparison of SNR. The goal of this section was to find the optimal parameters for ^{19}F MRI when using a spin echo sequence.

Typically, SNR was defined by the following equation:

$$\text{SNR} = \frac{S}{\sigma} \tag{11}$$

where the S was the signal intensity in the signal and the σ was the standard deviation of signal intensity in the noise (42,43). However, the noise influence on the signal was considered for lower signal strength imaging, such as ^{19}F MRI (15). In this case, the noise distribution was Rician instead of Gaussian, so additional changes were made. This meant the measured signal intensity in the magnitude images (S_m) was not equal to S. The mean S_m was written as:

$$S_m = \sqrt{S^2 + \sigma^2} \tag{12}$$

Solving for S, the equation becomes:

$$S = \sqrt{|S_m^2 + \sigma^2|} \tag{13}$$

For these lower SNR images, the new SNR equation was rearranged and written as:

$$\text{SNR} = \frac{\sqrt{|S_m^2 - \sigma^2|}}{\sigma} \tag{14}$$

Here, S_m was considered the signal intensity inside the signal ROI and σ was the standard deviation inside the noise ROI. The SNR derivations which include the Rician

noise were derived from (44). For high signal, as may be the case in the stronger phantom vial, the equation closely, if not exactly, represented the traditional SNR equation in that σ^2 may be negated. Additionally, a signal that has a voxel intensity magnitude larger than two and a half times the noise was considered significant by containing the actual ^{19}F signal.

IV.6.1 Observing T1-Weighted, Spin Density, and T2-Weighted Images

The first test was to determine which type of tissue contrast scan resulted in a higher signal for ^{19}F. The three common types to be considered were T1-weighted, T2-weighted, and proton density weighted images. The T1-weighted image eliminated the T2 effect by using a short TE value and enhanced the T1 effect by using a short TR value. The T2-weighed image used a long TR to reduce the T1 effect and a long TE to enhance the T2 effect. For spin density weighting, the T1 and T2 effects were eliminated by using a long TR and a short TE, respectively. These values were displayed in Table 2.

Table 2: Spin echo sequence combinations for T1-weighted, T2- weighted, and spin density images.

	TR (ms)	TE (ms)
T1- weighted	650	15
Spin density	2000	15
T2- weighted	2000	50

The strongest concentration phantom (yellow vial) was used for this experiment. To get an idea for localization of the vial in the scanner, hydrogen images were first taken (Fig. 18a). Then, with other constant parameters (voxel size 7.8x7.8x5.0 mm^3 and 32 averages), the TR and TE values were changed. The T1-weighted image is represented in Fig. 18b, the spin density in Fig. 18c, and the T2-weighted image in Fig. 18d.

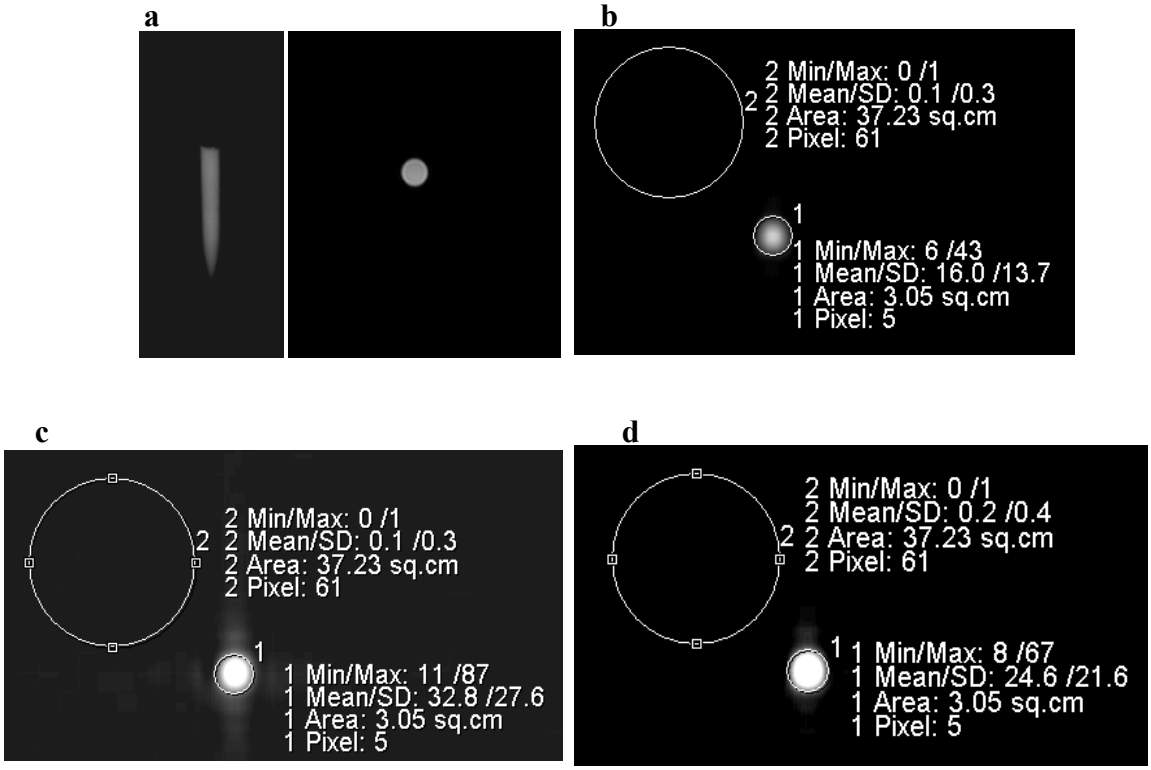

Figure 18: Spin echo sequence to observe fluorine-19. a) hydrogen localizer image. b) T1-weighted image for 19F. c) spin density weighted image for 19F. d) T2-weighted image for 19F.

The SNR values were observed in order to quantitatively compare the resulting images. The results were shown in Fig. 19. Spin density resulted in the highest SNR, with almost double the amount compared to the other two. This scan, however, appeared to have some artifacts surrounding the signal ROI. Because the SNR for the T1-weighted and T2-weighted image were closely comparable, it can be assumed that there was minimal difference between the two. An advantage of the T1-weighted image, however, is the largely reduced scan time.

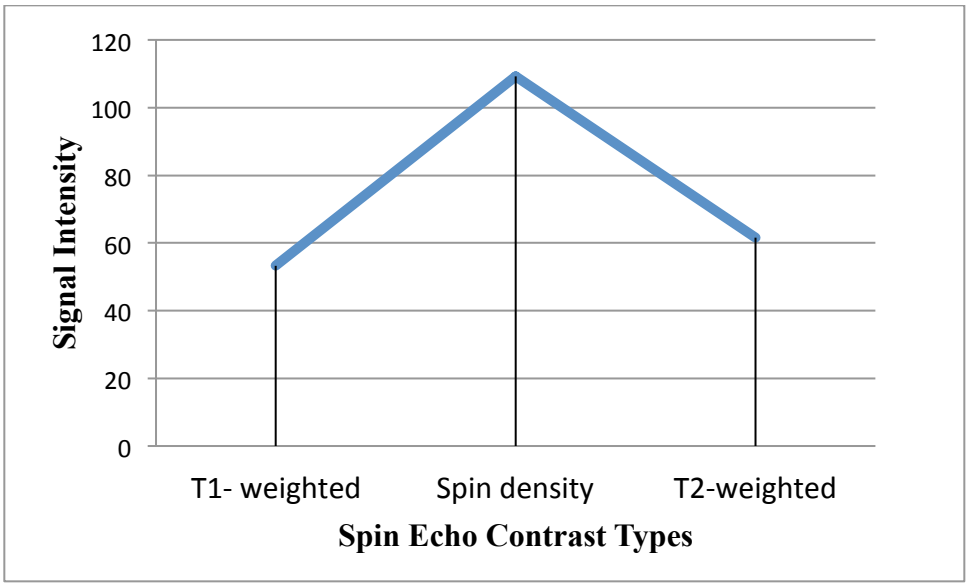

Figure 19: Resulting SNR comparisons for the different spin echo contrast types.

Additionally, with the use of spin density weighted images, it has been shown that one can estimate the number of cells with a known labeling efficiency (43). This will be furthered explored in Chapter IV.

IV.6.2 Quantification

Each Cell Sense phantom was imaged using the ideal parameters that implement a spin density weighted image with 32 averages, a matrix size of 64x64, and a large voxel size of 7.8x7.8x5.0 mm^3. The phantoms were imaged individually so placement location was consistent and signal loss would not occur if outside the isocenter of the coil. After images were acquired, they were analyzed by drawing ROIs around the signal for each slice acquired. These values were averaged and plotted to show the relationship between the number of spins and intensity of the signal (Fig. 20).

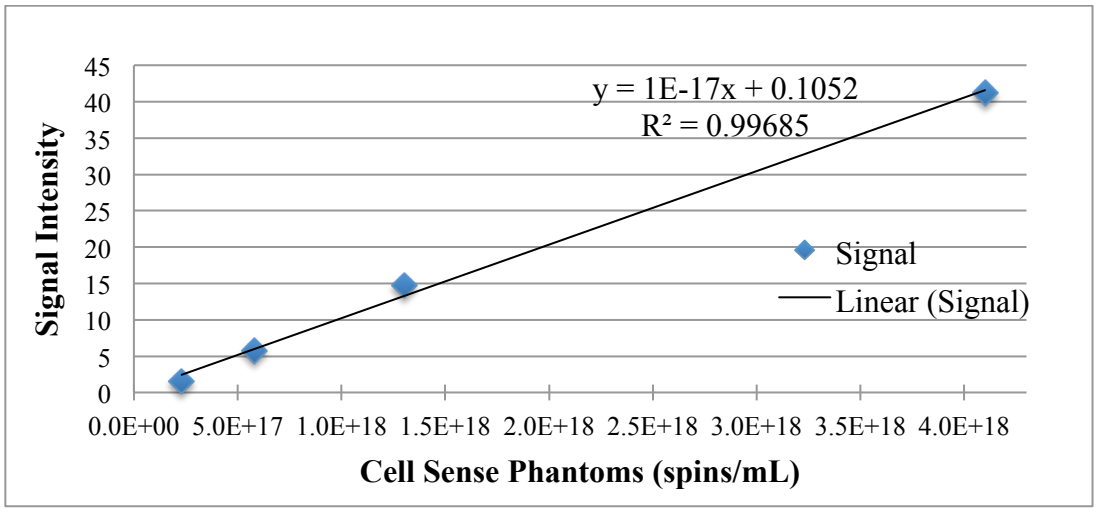

Figure 20: Spin echo sequence with voxel size of 7.8x7.8x5.0 mm^3 displaying the number of 19F spins per mL versus the signal intensity for the four different 19F concentration vials.

A linear fit graph was selected and plotted that resulted in a high coefficient of determination value, known as R^2, of 0.99685. The data points fit the linear statistical model as the R^2 value gets closer to one. The linear fit equation for the given parameters was:

$$\text{Signal Intensity} = (1\text{x}10^{-17})*(^{19}\text{F spins/mL}) + 0.1052 \quad (15)$$

These calculations showed there was a strong linear relationship between the signal intensity and the concentration of ^{19}F. This linear relationship between signal intensity and PFC concentration was also proven in previous studies (34,45).

The same experiment was repeated, except this time with a smaller voxel size of 3.9x3.9x5.0 mm^3 with a matrix size of 128x128 and a smaller TR of 1500 ms. For accuracy purposes, these parameters were repeated to match some of the earlier *ex vivo* cell experiments. The results were shown in Fig. 21.

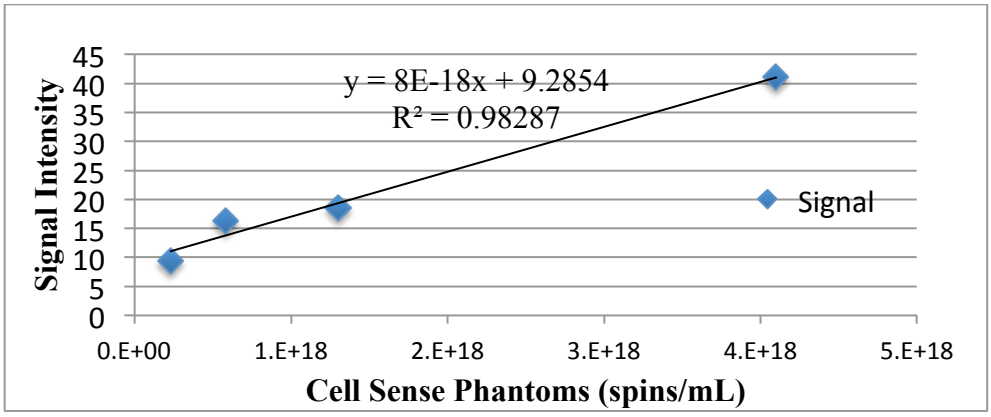

Figure 21: Spin echo sequence with voxel size of 3.9x3.9x5.0 mm^3 displaying the number of 19F spins per mL versus the signal intensity for the four different 19F concentration vials.

As before, a linear plot was fitted to the points with an R^2 value of 0.98287. The linear fit equation for the given parameters was:

$$\text{Signal Intensity} = (8\text{x}10^{-18})*(^{19}\text{F spins/mL}) + 9.2854 \quad (16)$$

Using this equation and the same imaging parameters, the signal intensity or the number of 19F spins can be predicted for future studies. These two calculations proved there is a strong linear relationship between the signal intensity and the concentration of ^{19}F.

CHAPTER V

MULTINUCLEAR FLASH

A gradient echo (GRE) is another common, simple pulse sequence but differs from SE in that the flip angle for GRE is usually less than 90° and there is no 180° RF rephrasing pulse. This sequence used a magnetic field gradient to induce the formation of an echo.

There are different types of gradient echo techniques and the different scanner manufacturers have come up with different names for each type of imaging. Since the research conducted in this thesis uses a Siemens MRI scanner, the Siemens' term FLASH, which stands for Fast Low Angle Shot, will be used for this type of sequence. The FLASH sequence was first introduced by Haase in 1986 and allowed for fast acquisition of MR images (46). This type of gradient echo incorporates elimination or "spoiling" of the steady state transverse magnetization.

Spoiling of the residual transverse magnetization leaves only the longitudinal component affecting the signal. This technique can be accomplished in three methods. The first way is RF spoiling, which adds a phase offset to each RF pulse and a corresponding phase shift in slice select vectors. The second method to spoil the steady state transverse magnetization is by adding gradient spoilers. Finally, increasing TR can be used to achieve spoiling because it allows for adequate dephasing of the spins in the transverse plane.

The advantages of using FLASH sequences are resulting images with enhanced image contrast and fast image acquisition. However, FLASH sequences are susceptible to magnetic field inhomogeneities.

The main set up for this sequence has one RF pulse, gradient pulses in the x-, y-, and z-direction, and an ADC signal detection readout.

V.1 Radiofrequency Pulses

The RF pulse used in this FLASH sequence is a SINC pulse and is expressed mathematically as:

$$\text{sinc}(t) = \frac{\sin(t)}{t} \tag{17}$$

A SINC pulse is a common RF pulse used in MRI because its Fourier transform is a simple rectangle. This means the excited tissue will be under the rectangle shape where the edges between slices can be as sharp as possible. Additionally, this SINC waveform has 128 samples (or points) and is a Hanning filtered pulse. Siemens requires the number of samples must divide evenly into the pulse duration.

The time-bandwidth (TBW) product, which is a unitless value, defines the bandwidth of a SINC pulse. This number is given by:

$$TBW = T\Delta f = N_L + N_R \tag{18}$$

The time-bandwidth product can be found two ways. The first is the product of the duration of the SINC pulse and the bandwidth of the pulse in Hertz. For this sequence, the pulse has a total duration of 2.56 milliseconds. The maximum allowed duration for an RF pulse is 100 milliseconds, and the sequence will not run if the duration exceeds this value. The equation below defines the corresponding frequency:

$$\Delta f = \frac{1}{t_0} \tag{19}$$

where t_0 represents one-half the width of the central lobe (as shown in Fig. 22). The t_0 value for this symmetric SINC pulse with no negative lobes is half the duration, or 1.28 milliseconds. This makes Δf equal to 781.25 Hz. The TBW is then 2.56 milliseconds multiplied by 781.25 Hz, which equals 2. It should be noted that the calculations use absolute Hz; therefore, the formula is independent of magnetic field strength. The second method for solving for the TBW is adding the number of zero crossings in the SINC pulse to the left and right of the central peak, N_L and N_R, as indicated in Eq. 18. Because this SINC pulse displayed in the FLASH sequence has no negative lobes, the number of zero crossing, $N_L + N_R$, equals 2. The equations above were derived from (47).

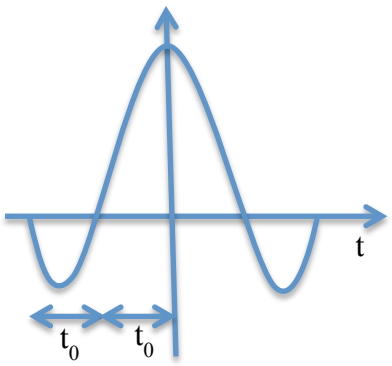

Figure 22: General SINC pulse showing each lobe is denoted as t_0.

V.2 Gradients

The three main gradients are the slice select, phase encoding, and readout. Additionally, spoiler gradient are added in the slice select and readout directions. As in Chapter IV, the gradients in the FLASH sequence follow the same trapezoidal shape. Recall that when referring to gradient duration, this time is the ramp up time plus the flat top time. Due to scanner qualifications, the gradient timings, including ramp times, must be a multiple of 10 microseconds.

V.2.1 Slice Select

There are three main gradients in the slice select direction: the slice select gradient, its accompanying rephasing gradient, and a spoiler gradient. The slice select gradient is turned on during the activation of the RF SINC pulse. It converts the frequencies of the RF pulse into their corresponding slice locations. Similarly, as explained in Chapter IV, the slice select gradient will have the necessary amplitude to achieve the requested slice thickness given the bandwidth of the RF pulse. This is an automatic process that is retrieved from the RF pulse object and can be shown mathematically by:

$$G_{SS} = \frac{\mathrm{TBW} * 10^6}{\gamma * \mathrm{RF}_{\mathrm{DUR}} * ST} \tag{20}$$

where G_{SS} is the magnitude of the slice select gradient in mT/m , TBW is the time-bandwidth product, ST is slice thickness in millimeters, RF_{DUR} is the SINC RF duration in microseconds, and γ is the gyromagnetic ratio of fluorine-19 in MHz/T. Therefore, if the slice thickness is increased, then the slice select amplitude will decrease for a constant RF duration.

The slice rephasing gradient has the same set-up as in Chapter IV. This gradient has opposite polarity of the slice select gradient. The area of the slice rephasing gradient equals the area of the slice excitation gradient starting at TE=0 (or the middle of the SINC RF pulse) to the end (Fig. 23). The gradient has the maximum amplitude possible with the shortest rise time in order to rephase the excited spins.

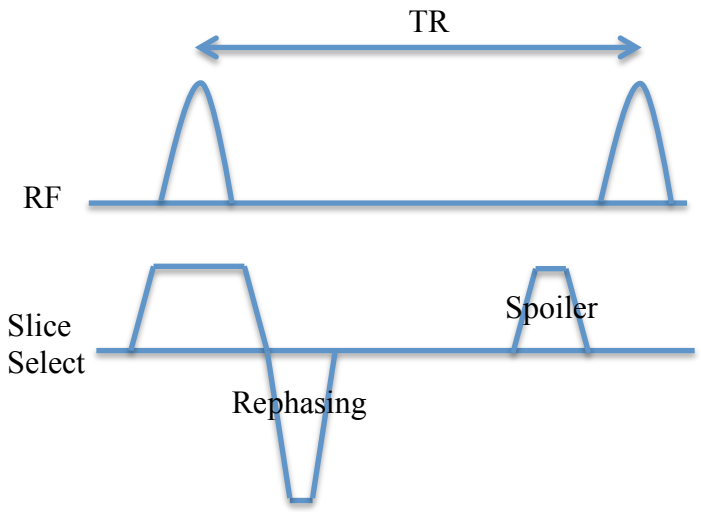

Figure 23: FLASH RF pulse and its slice select gradients.

The spoiler gradient in the slice select direction has an area that is half of the slice select gradient. This gradient has the same polarity as the slice select gradient in efforts to reduce eddy currents and has constant amplitude in order to reduce the residual transverse magnetization (48).

V.2.2 Phase Encoding

In the phase encoding direction, the two gradients applied are the phase encoding table gradient and the phase encoding table rewinder gradient (Fig. 24). The phase encoding table implements different phase variations while the area under the trapezoidal gradient changes from positive to negative or vice versa.

The phase encoding table rewinder gradient is set up exactly like the phase encoding table gradient with equal magnitude except with opposite polarity. The polarity for the phase encoding table starts off positive, therefore, the polarity for the phase encoding rewinder starts off negative. This gradient is used in addition to the RF spoiling and enables transverse coherences, which will aid in the improvement of SNR. This rewinder gradient was found to be effective in reducing horizontal band artifacts (49).

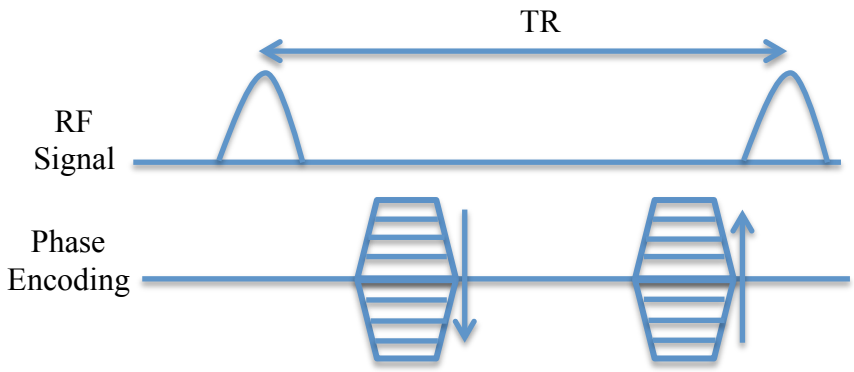

Figure 24: FLASH sequence showing RF pulses and the phase encoding table and rewinder.

V.2.3 Readout

The frequency encoding direction contains the readout gradient, the readout dephasing gradient, and a spoiler gradient (Fig. 25). In order to form an echo in the absence of a 180° pulse, the FID is intentionally dephased and then rephased at TE. The readout gradient and readout dephasing gradient accomplish this. The readout dephasing gradient dephases the spins in the transverse plane thus eliminating the FID. Then the positive readout gradient rephases the spins and creates the FID with stronger signal in a readable echo.

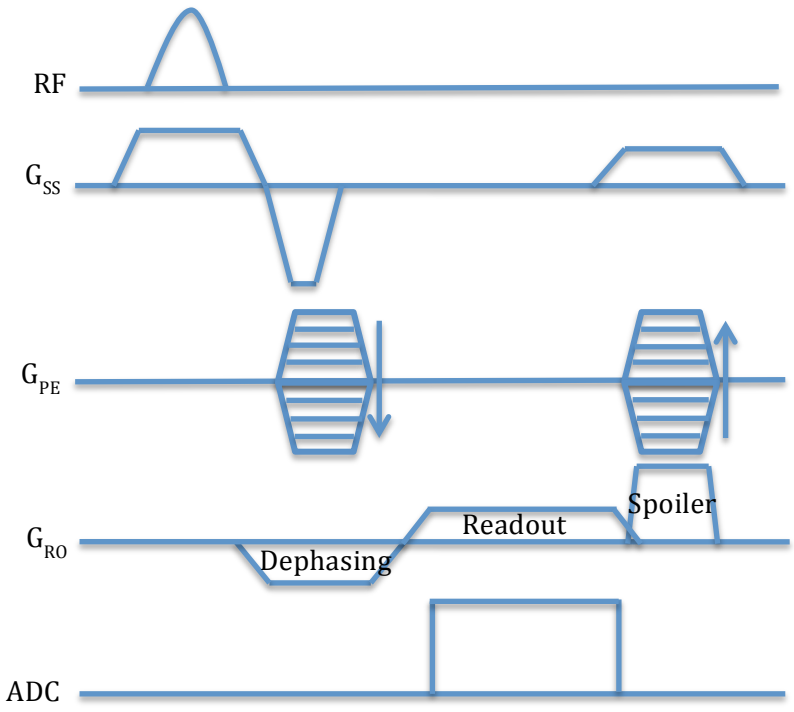

Figure 25: Complete FLASH sequence.

The readout gradient has a duration derived from the ADC object, and is equal to the readout gradient ramp up time plus the ADC duration. The readout dephasing gradient has area equal to the readout gradient up to TE (or half the area of the readout gradient assuming symmetric sampling).

As stated previously, the purpose of the spoiler gradient is to eliminate residual transverse magnetization that occurs at the end of a pulse sequence, which could potentially cause image artifacts. This residual transverse magnetization may affect the next RF pulse because the TR may be too short to allow for complete dephasing of the spins in the transverse plane. The readout gradient and the spoiler gradient overlap in time, and their points add together to form the combined amplitude. This amplitude must still not exceed the maximum limits.

V.3 ADC Object

The ADC object converts the time varying analog signal into a digitized form consisting of 0s and 1s that the computer recognizes. Its goal is to sample a signal and reconstruct the original signal from just the samples.

As described in the spin echo section, the columns, dwell time, and bandwidth define the ADC object. The columns are defined by the base resolution defined by the user. The dwell time is the time between successive sampling points and is calculated by the inverse of the Nyquist frequency for an image field of view (FOV). This means ADC duration is the base resolution, or number of columns, multiplied by the time in between each column, or dwell time. The bandwidth is the reciprocal of the total sampling time, and has a default value of 130 Hz/pixel. Typically, a normal FLASH sequence would

have a higher bandwidth (around 390 Hz/pixel). Because this is a multinuclear scan, the bandwidth is narrower in hopes of increasing SNR.

V.4 Multinuclear Option and Other Parameters

Similar to the set up for multinuclear in SE, the scanner and FLASH sequence must have the capabilities for mulitnuclear. The scanner must be multinuclear compatible, meaning that it is able to recognize nuclei other than hydrogen. Additionally, the multinuclear option must be enabled in the sequence. It is possible to make one sequence compatible with all available nuclei or make one sequence focus primarily on the nuclei of choice. The sequence created in this thesis is only applicable to ^{19}F and ^{1}H, not any other nuclei. This is because ^{19}F has a higher gyromagnetic ratio (only 6% different than that of hydrogen) compared to other nuclei so some changes were not applicable here. For nuclei with lower gyromagnetic ratio, the gradient strength must be increased. An example would be to increase the phase encoding gradient durations and ramp times. Another multinuclear addition to be made is adding two libraries to the FLASH makefiles. Makefiles are required files when programming in SDE and contain the libraries the C++ code plans to use. Therefore, in order for the C++ code to recognize the change of nucleus from ^{1}H to ^{19}F, its makefiles must contain the necessary libraries. These libraries contain important information, such as the gyromagnetic ratio, on the other nuclei.

Additionally, the coil set up remains the same for the FLASH as it did with the SE sequence. This ^{19}F coil was purchased from RAPID Biomedical (as described in Chapter III), along with the necessary coil and plug files.

The RF spoiling in this sequence is an option that is enabled to activate the FLASH sequence. It eliminates the steady-state transverse magnetization. To do this, the phase of the transmitter and receiver is incremented by a fixed amount with each TR cycle. This method requires the use a phase encoding rewinder gradient because the gradient areas on the x-, y-, and z-axis must be spatially independent (not vary from one TR cycle to the next).

There are three main factors that affect contrast for a FLASH sequence: the flip angle, TE, and TR. The flip angle for this sequence needs to be an angle smaller than 90° if using a small TR because a small flip angle results in a large amount of longitudinal magnetization (Fig. 26).

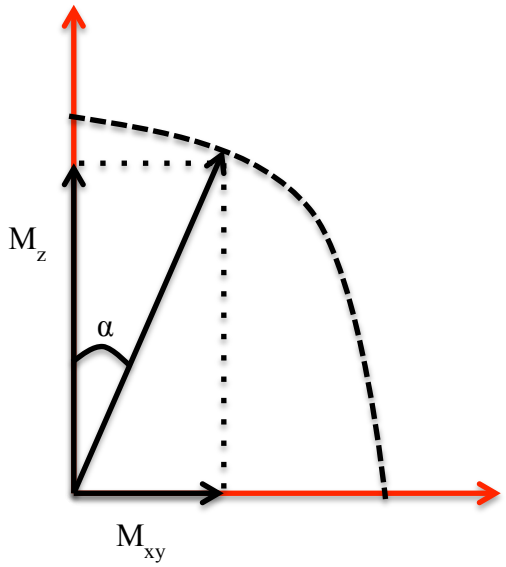

Figure 26: Relationship between the flip angle, α, and the transverse and longitudinal magnetization.

For this study, the flip angle was varied for comparison purposes. If a higher flip angle were used, such as a 90° RF pulse, with a small TR then the longitudinal magnetization would not have sufficient time to recover. This would cause a substantial decrease in the longitudinal magnetization and transverse magnetization, thus resulting in lower amplitude of the received signal. This would lower SNR dramatically, which is non-ideal and impractical in multinuclear imaging. A small flip angle for a FLASH sequence produces a spin density weighted image. The signal intensity (SI) equation for FLASH suggested by Weber et al. is shown in Eq. 21 (50) where n is the proton density and α is the flip angle.

$$\mathrm{SI} = \mathrm{n}\, e^{-\frac{TE}{T2*}} \frac{\left(1 - \mathrm{e}^{-\frac{\mathrm{TR}}{\mathrm{T1}}}\right)\sin\alpha}{\left(1 - \cos\alpha\, \mathrm{e}^{-\frac{\mathrm{TR}}{\mathrm{T1}}}\right)} \tag{21}$$

This shows that for large flip angles and short TR values, the image resembles T1-weighted scan.

The minimum TR required is found by adding half of the slice select gradient total time, the TE value in the protocol, half of the ADC duration, and the longer time duration between the phase encoding rewinder gradient and the slice select spoiler gradient. If this minimum TR is larger than the TR in the protocol then it will be rejected and an error message will be displayed. For a short TR, there will not be complete transverse magnetization decay before the next RF pulse. As TR is increased, the T1 weighting of the image is enhanced. However, as TR is increased, the scan time is also increased.

The minimum TE required is found by adding half the RF pulse duration, the ramp up time for the readout gradient, half the ADC duration, and finding the longest gradient between the readout dephasing gradient, the phase encoding table gradient, and the slice select rephasing gradient. Like with TR, the minimum TE is compared with the TE from the protocol and if the minimum TE is larger then an error will occur. TE plays a similar role in FLASH sequences as it does in SE sequences. A short TE enhances T1-weighted or spin density weighted imaging.

V.5 Virtual Simulation

After successful compilation of the multinuclear pulse sequence C++ code and its necessary make files, a unit test was performed to test various parameters and sequence timings. The unit test was successful (Fig. 27) and displayed as an HTML file. The coil and plug files from RAPID Biomedical were copied to the customer coil file section in IDEA. Then the virtual coils were edited to select for the 19F/1H surface flex coil. The same method as described in the spin echo chapter was used for enabling the customer coil and plug files in POET.

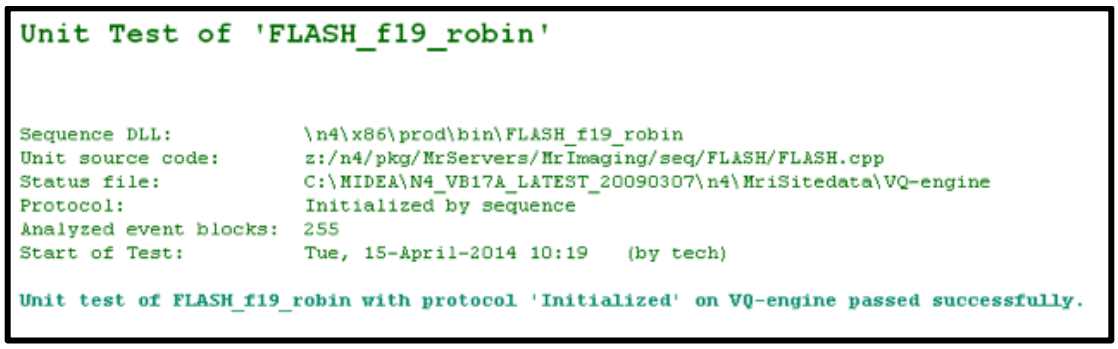

Figure 27: Successful unit test for the multinuclear FLASH sequence.

A graphical pulse sequence in POET was obtained to make sure the RF pulse, the gradients, and ADC were positioned and calculated correctly (Fig. 28).

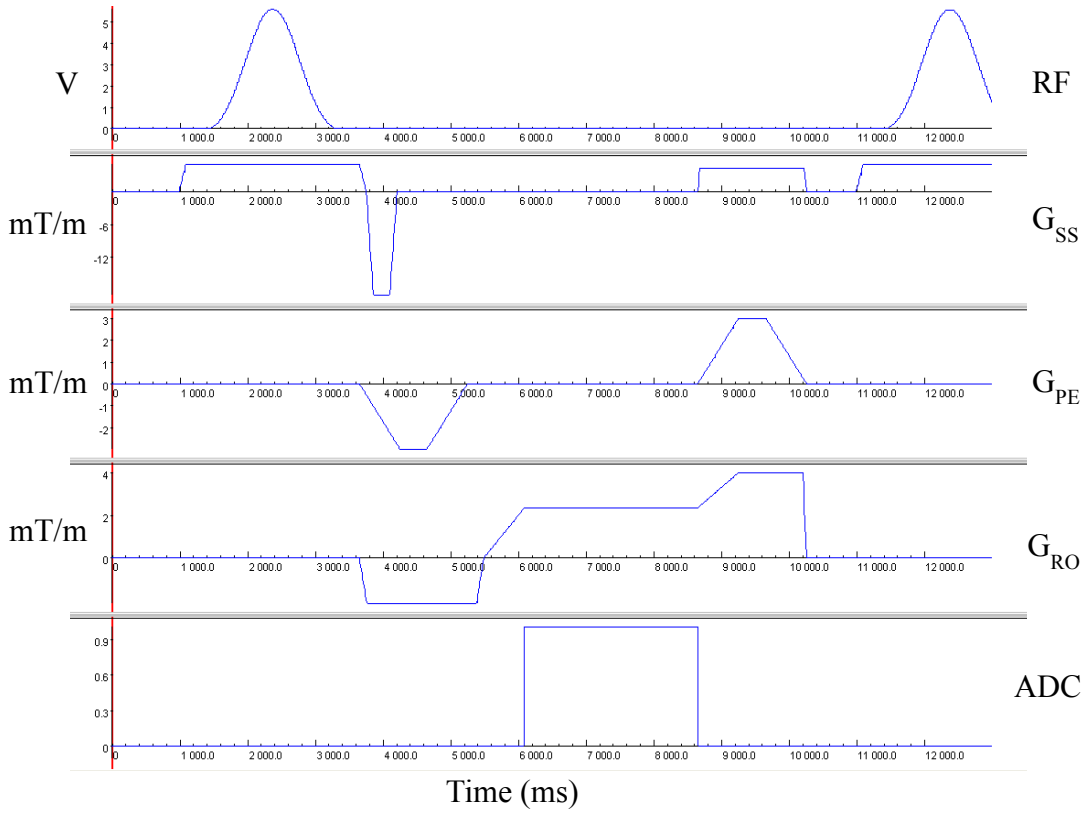

Figure 28: Virtual FLASH sequence shown in POET.

The parameters used for this simulation was 10 slices at 20% distance factor with transversal orientation, voxel size of 3.9x3.9x5.0 mm^3 with TR of 10 ms and TE of 5 ms. This graph shows the first RF pulse and the beginning of another. The slice select gradient is properly lined up with the RF pulse followed by the steep rephasing gradient and the spoiler located at the end of the TR cycle. The phase encoding gradient starts off negative while the phase encoding rewinder has opposite polarity. Over time these gradients will change polarity and the phase encoding gradient will be positive while the rewinder will be negative. The readout gradient and its followed spoiler gradient are

adding in amplitude for the overlapped sections, as described earlier. The ADC is correctly lined up with the readout gradient.

V.6 Cell Sense Phantom Imaging

The same phantoms imaged in the spin echo pulse sequence were imaged in this sequence for comparison. The goal of this section was to find the best parameters suitable for fluorine-19 MR imaging for future studies.

SNR was calculated the same way as in Chapter IV. First, a region of interest (ROI) was drawn around the signal containing the ^{19}F. Another ROI was drawn around the outside area containing the noise. SNR was calculated to be:

$$\text{SNR} = \frac{\sqrt{|S_m^2 - \sigma^2|}}{\sigma} \tag{22}$$

where S_m represented the measured signal intensity in the magnitude ROI and σ was the standard deviation of the noise ROI. A signal that has a pixel intensity magnitude larger than two and a half times the noise was considered significant to contain the actual ^{19}F signal.

V.6.1 Observing TR and Matrix Size

Different TR values were compared against matrix sizes. First, hydrogen images of the 4 Cell Sense phantoms were taken for localization purposes (Fig. 29). The order for this scan was increasing fluorine concentration when going from top to bottom vial. For instance, the top vial was the blue phantom, which has the least amount of fluorine, and the bottom vial was the yellow phantom, which contains the largest fluorine concentration. Additionally, a region of interest was drawn around one vial in order to

know its approximate area. Two rulers were drawn to determine distance from consecutive vials and total distance spanning the four vials. The goal of this was to provide an idea of placement when scanning the fluorine images.

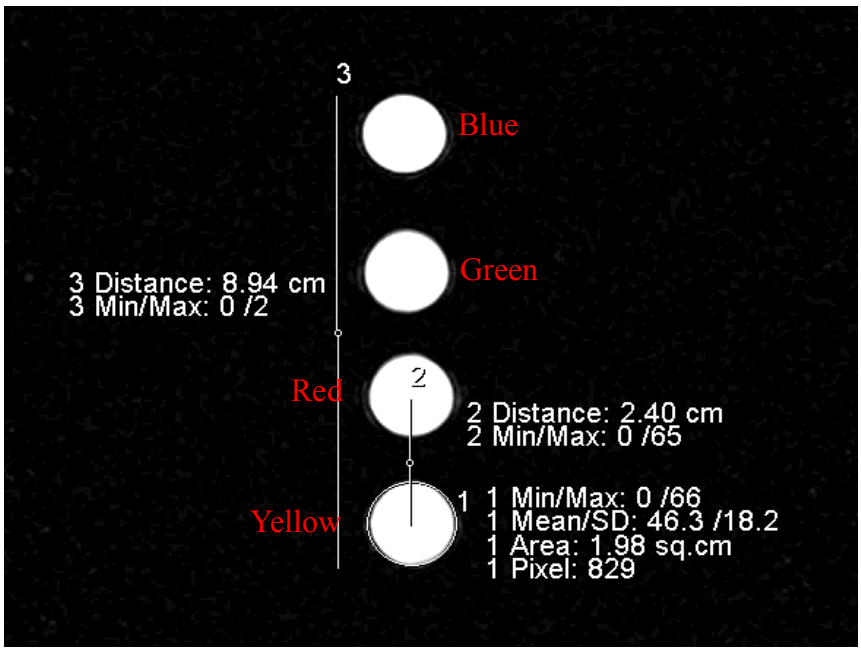

Figure 29: Hydrogen localizer of the 4 Cell Sense phantoms. Two rulers were drawn to show the relative distance.

In the fluorine scans, two TR values (10 ms and 100 ms) were compared against two different matrix sizes (128x128 and 256x256), while other parameters were kept constant (TE of 5 ms, 32 averages, 400 mm field of view, 5 mm slice thickness). Fig. 30a represents the phantoms when imaged with a TR of 10 ms and matrix size of 128x128. Only the yellow and red phantoms were visible in this scan. A ruler was drawn from the middle of the yellow vial to the middle of the red vial to measure distance for comparison to the localizer measurements. Two large circular ROIs were drawn around the approximate section containing the vial with two smaller circles drawn around the strong signal detection. It was these smaller circles that will be used in the SNR calculation, as well as the largest circular ROI that represents noise. This same pattern will follow for the remaining three images in this experiment. Fig. 30b has a TR of 100 ms and matrix size of 128x128. There was a small white bright spot above the red phantom that most likely represents the green phantom. However, its signal intensity was not statistically significant, meaning the intensity was not at least two and a half times the noise mean intensity. Therefore, it was excluded from these SNR calculations.

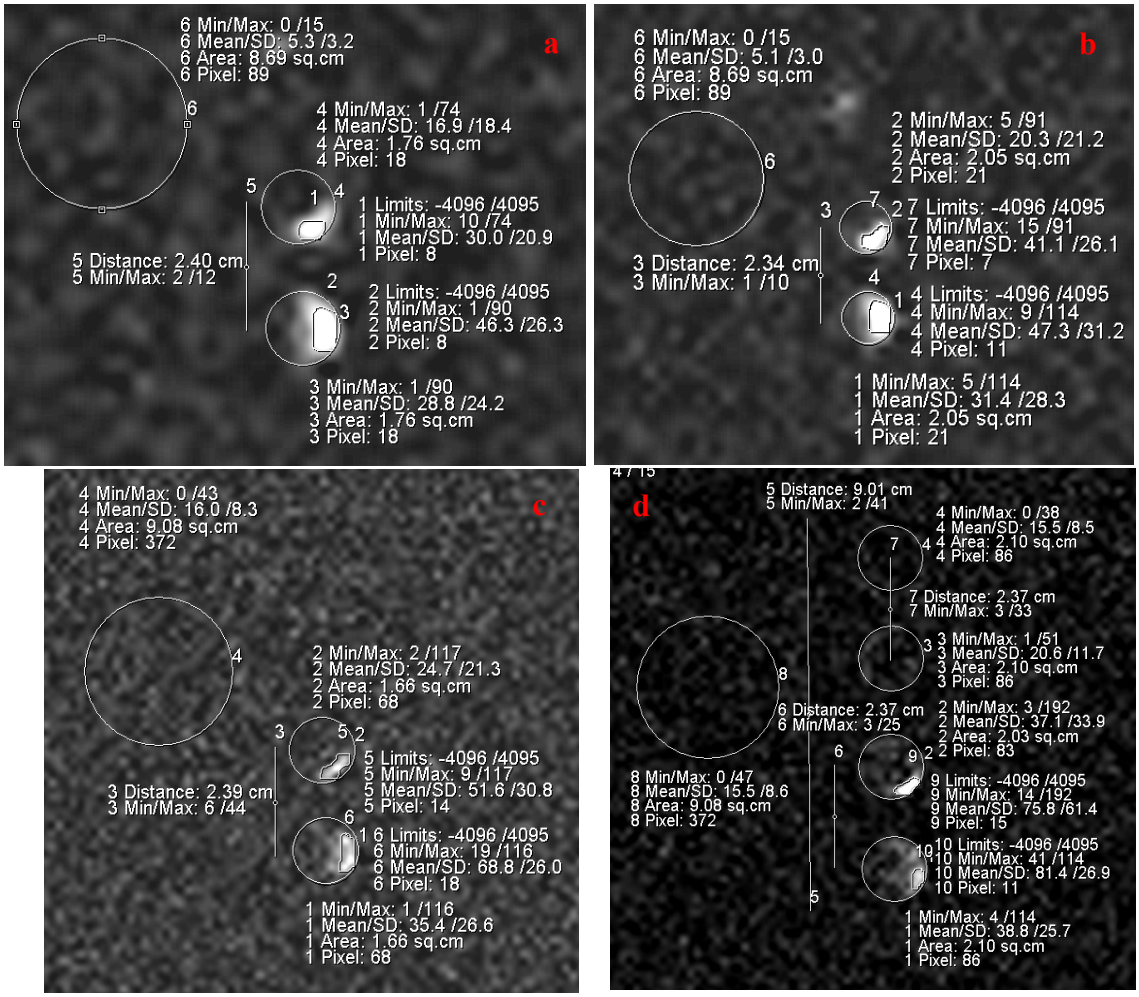

Figure 30: FLASH sequence of ^{19}F MRI used to compare TR and matrix size. a) TR of 10 ms and matrix size of 128x128. b) TR of 100 ms and matrix size of 128x128. c) TR of 10 ms and matrix size of 256x256. d) TR of 100 ms and matrix size of 256x256.

A TR of 10 ms and matrix size of 256x256 was evaluated in Fig. 30c, and an increased TR of 100 ms with the same 256x256 matrix size was compared (Fig. 30d). The same set-up was conducted in these scans as the previous, except in Fig. 30d, two additional

ROIs were drawn to show the approximate location of the blue and green vials. As before, these regions were statistically unimportant and were ignored.

For additional experimental and comparison purposes, a TR of 100 ms and matrix size of 64x64 was imaged (Fig. 31). The results thus far proved that a higher TR was more likely to increase SNR, so only a TR of 100 ms was observed. The matrix size was lowered to 64x64 to observe quality and the possibility of artifacts.

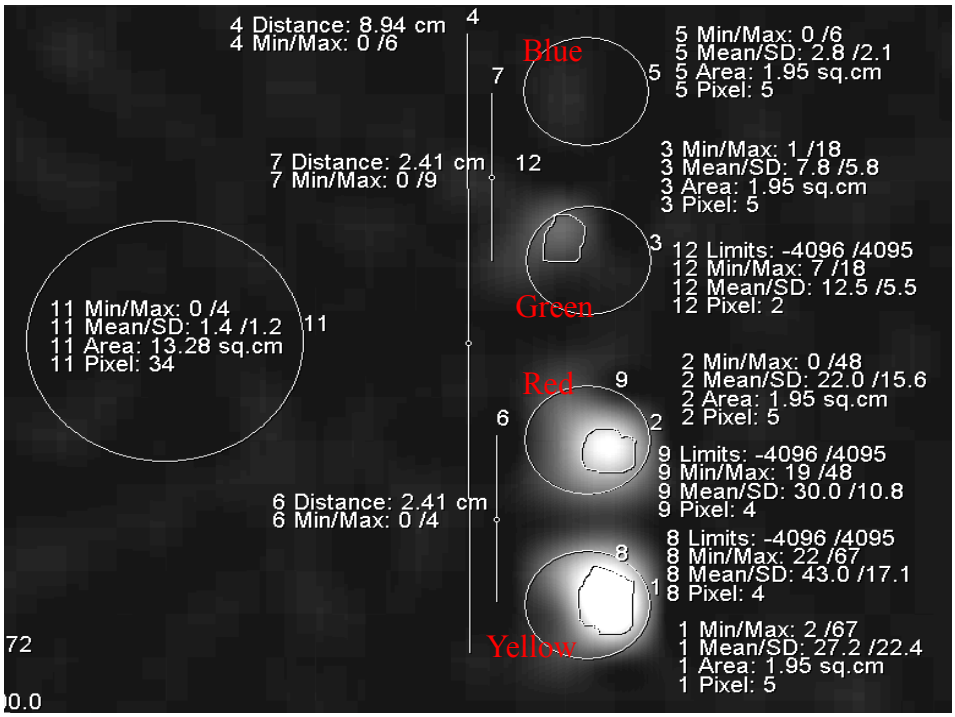

Figure 31: FLASH sequence ^{19}F MRI with TR of 100 ms and matrix size of 64x64.

As before, circular regions were drawn, along with rulers to measure accuracy and compare it to the hydrogen localizer, to represent the different phantoms. Unlike the

previous results shown in Fig. 30, the green vial was visible and had a signal intensity mean greater than two and a half times the noise mean ROI. This means the signal was significantly significant and can be considered fluorine signal. Additionally, without adjusting contrast of the image, this image appears to contain the most visibly bright regions and thus appears to detect the fluorine on a more comparable standard. It also results in a higher signal with a smaller value of noise compared to the previous tests.

The previous two figures were compared quantitatively in Fig. 32. SNR values, found by calculating signal mean pixel intensity ROI divided by standard deviation of the noise mean pixel intensity ROI, showed that a larger TR with the smaller matrix size obtained the largest amount of detected fluorine-19 inside the phantoms.

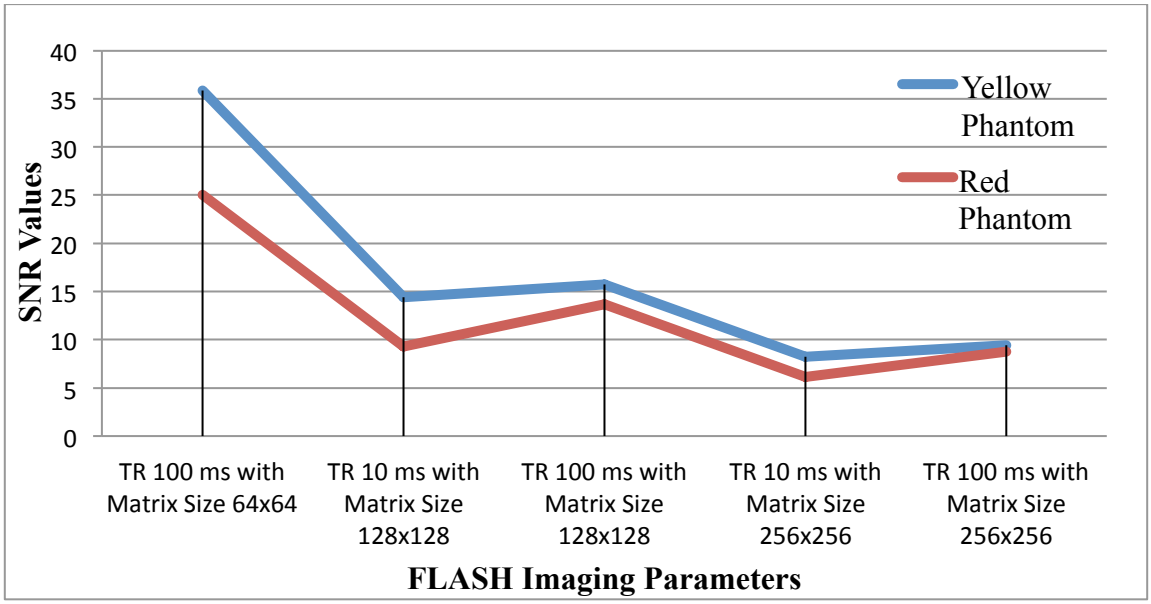

Figure 32: Quantitative comparison of TR of 10 ms versus 100 ms and matrix size of 256x256 versus 128x128 versus 64x64 in the ^{19}F MRI FLASH sequence.

The larger TR was ideal because it allowed the spins to have more time to relax before the next RF pulse. Unfortunately, this increase of TR meant a longer acquisition time, which may be illogical for certain preclinical or clinical studies. Additionally, the larger voxel size allowed higher signals to be received by each individual pixel.

V.6.2 Observing TE

First, hydrogen scans were taken, as shown in Fig. 33a. The vials were roughly 8 cm long, so rulers were drawn in the fluorine images to verify that the signal is coming from within the vial and not outside artifact. Constant parameters used were voxel size of 7.8x7.8x5.0 mm^3, TR of 100 ms, 16 averages, matrix size of 64x64, and scan time of roughly 34 minutes. Fluorine-19 images with TE values of 5 ms and 20 ms were scanned displayed in Fig. 33b and Fig. 33c, respectively. It is clear that as the TE increases, the artifacts surrounding the phantom vials became more apparent, as explained previously. The shorter TE image was also more precise with less noisy and pixelated regions next to the phantoms.

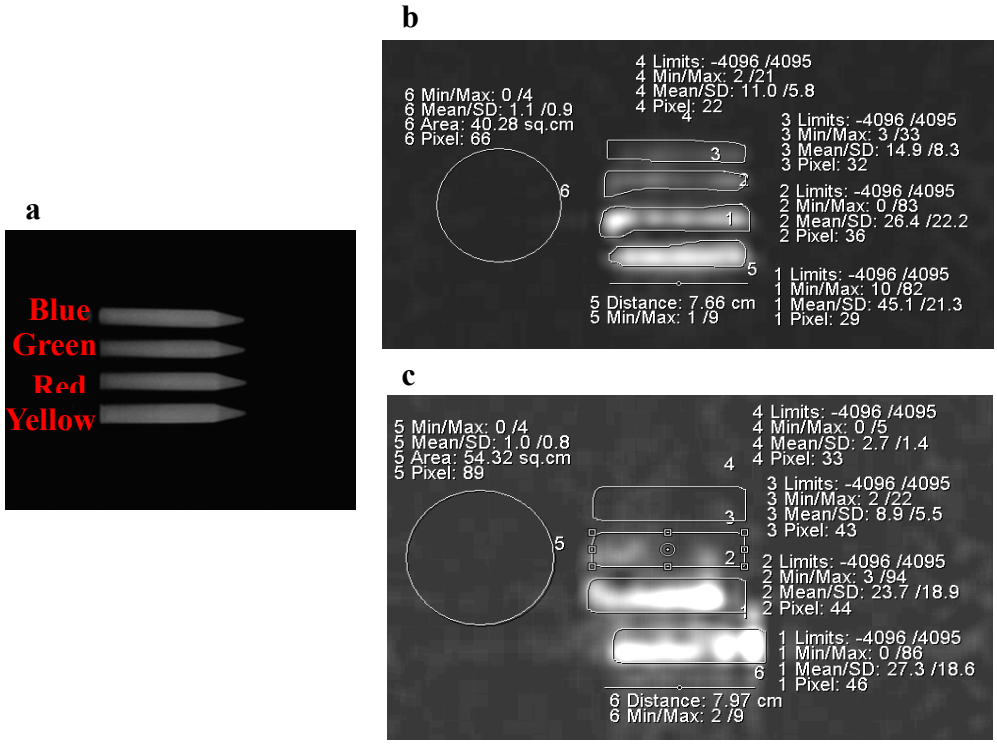

Figure 33: FLASH sequence comparing TE values for ^{19}F MRI. a) Hydrogen localizer showing the four different Celsense phantoms in increasing fluorine concentration going from top to bottom. b) TE value of 5 ms. c) TE of 20 ms.

A shorter TE proves to be more ideal in a FLASH sequences (Fig. 34). This is because FLASH sequence is sensitive to field inhomogeneites due to it lacking rephasing pulses. This makes the image T2* contrast instead of T2 contrast. These distortions- called susceptibility artifacts- can cause signal voids, which result in a loss of image information. The severity of the signal voids is related to the TE used. When a large TE is used, the signal voids are more pronounced. As expected, these results also show the relationship between fluorine concentration and signal intensity. Additionally,

field strength can play a role in this analysis, and the higher field strength produces a more obvious spin dephasing and, thus, signal voids.

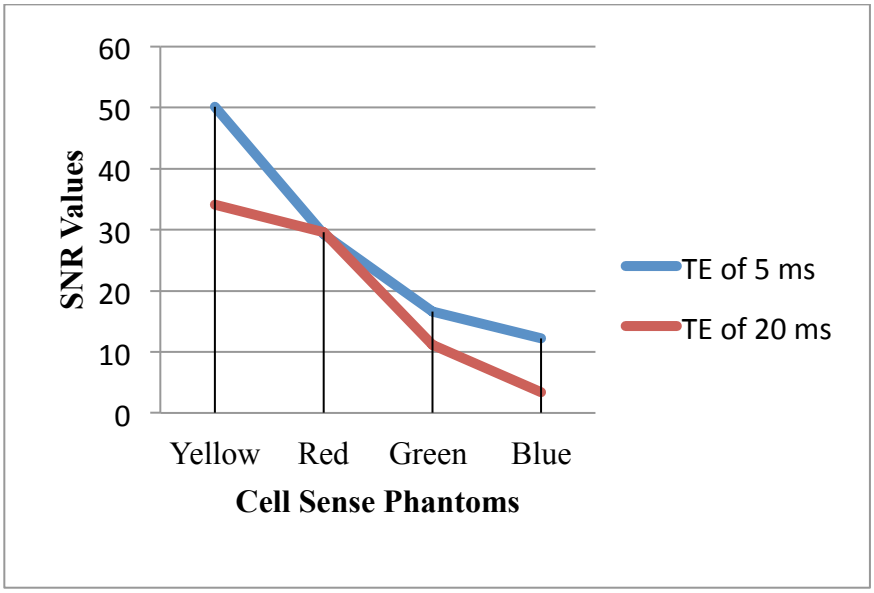

Figure 34: 19F MRI of FLASH sequence comparing TE values of 5 ms and 20 ms for the four different Celsense phantom vials.

V.6.3 Observing Flip Angle

For comparison, the flip angle of the FLASH sequence was observed. For this experiment, just the strongest fluorine concentration vial (yellow) was used. Fig. 35a has a flip angle of 15°, while the flip angle was increased to 75° in Fig. 35b. The SNR for the 15° flip angle was calculated to be 229.25, and the 75° flip angle has a SNR of 117.75.

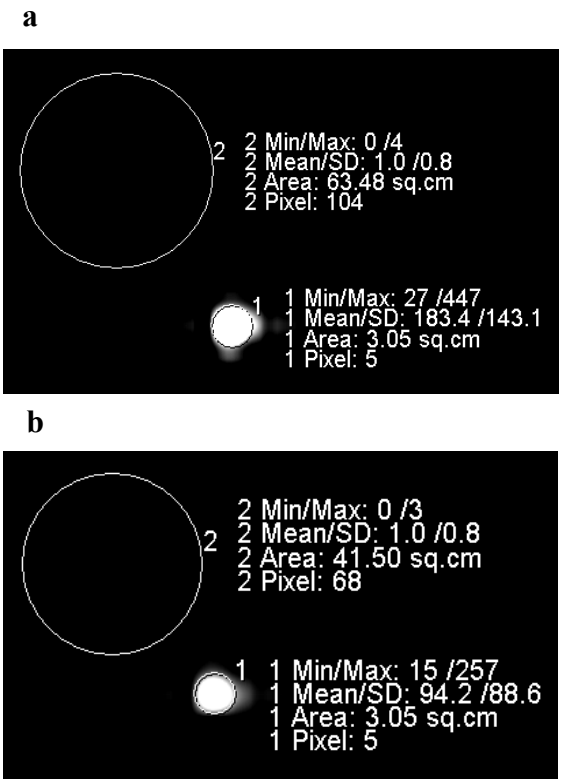

Figure 35: Comparing the flip angle in FLASH sequence. a) Flip angle of 15 degrees. b) Flip angle of 75 degrees.

The smaller flip angle results in the larger amount of longitudinal magnetization. Additionally, the smaller flip angle results in a spin density type image, which was already proven in Chapter IV to result in a higher SNR. For the remaining studies, the flip angle when using the FLASH sequence will be set to 15 degrees.

V.6.4 Quantification

Similar to the analysis in the spin echo section, each Cell Sense phantom was imaged using the ideal parameters found for the FLASH sequence that include TR of 100 ms, TE of 5 ms, 15° flip angle, a matrix size of 64x64. Slice thickness of 5 mm was

used creating a large voxel size of 7.8x7.8x5.0 mm^3, along with 32 averages. As explained before, the phantoms were imaged individually so location was consistent and signal loss would not occur if outside the isocenter of the coil. After images were acquired, they were analyzed by drawing ROIs around the signal for each slice acquired. These values were averaged and plotted to show the relationship between the number of spins and intensity of the signal (Fig. 36).

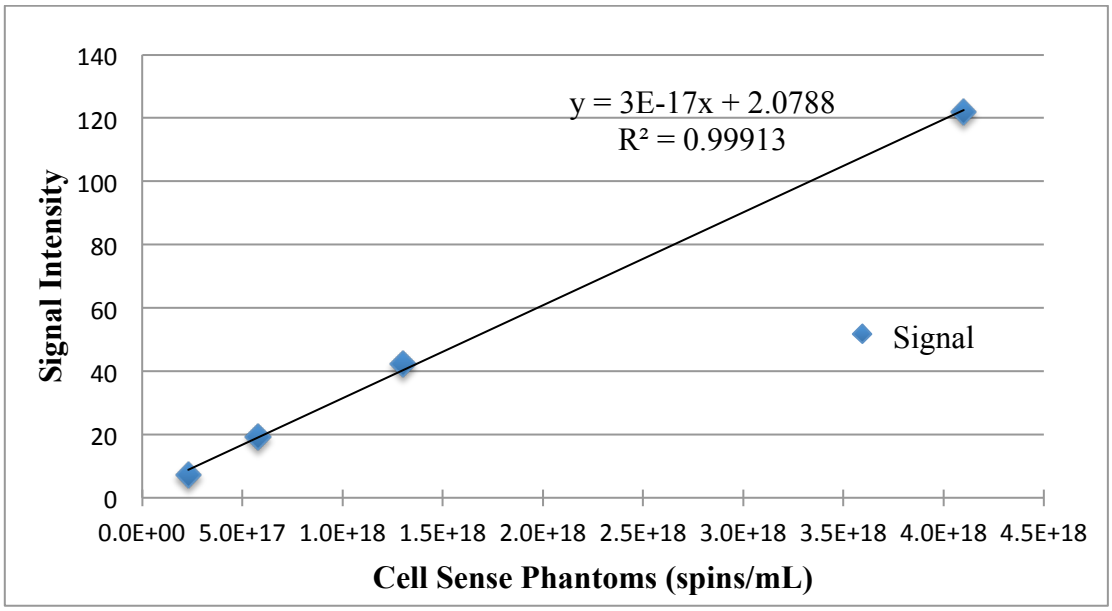

Figure 36: FLASH sequence with voxel size of 7.8x7.8x5.0 mm^3 displaying the number of 19F spins per mL versus the signal intensity for the four different 19F concentration vials.

A linear fit graph was selected and plotted that resulted in a high coefficient of determination value (or R^2 value) of 0.99913. With this value of R^2, the linear fit is a

suitable statistical model for the data points. The linear fit equation for the given parameters was:

$$\text{Signal Intensity} = (3\text{x}10^{-17})*(^{19}\text{F spins/mL}) + 2.0788 \quad (23)$$

This equation was used to estimate the amount of ^{19}F spins or the predicted signal intensity.

The same experiment was repeated, except this time with a smaller voxel size of 3.9x3.9x5.0 mm^3 with a matrix size of 128x128. For accuracy purposes, these parameters were repeated to match some of the earlier *ex vivo* cell experiments. The four phantoms were plotted with a linear fit (Fig. 37).

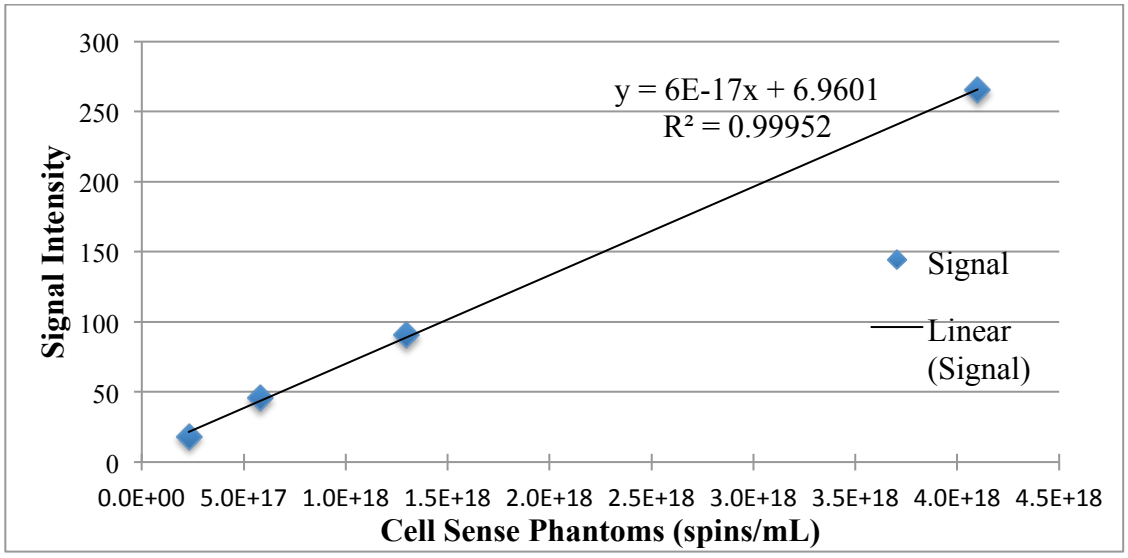

Figure 37: FLASH sequence with voxel size of 3.9x3.9x5.0 mm^3 displaying the number of 19F spins per mL versus the signal intensity for the four different 19F concentration vials.

As before, a linear plot was fitted to the points with an R^2 value of 0.99952. The linear fit equation for the given parameters was:

$$\text{Signal Intensity} = (6\text{x}10^{-17})*(^{19}\text{F spins/mL}) + 6.9601 \quad (24)$$

This equation was used for the *ex vivo* cell measurements in the following chapter. Also, because the parameters to match a spin density weighted image were used, the resulting image and its signal intensity can predict the amount of ^{19}F spins. This proven linear relationship between the concentration of fluorine and the signal intensity can prove useful in determining the needed amount of fluorine when doing *in vivo* studies.

CHAPTER VI

EX VIVO IMAGING

The fluorine-19 labeled cells were created by Dr. Colleen O'Connor at Division of Pediatrics at the University of Texas MD Anderson Cancer Center. Her work showed that the add-back of T cells after chemotherapy improves outcomes with a tumor-free survival (51). Client-owned canines were chosen because they closely model human malignancies by their similar genetic make-up, large size, tumor structures, and current treatments (52-57). A clinical problem with cellular immunotherapy in humans is the tracking of infused cells. It is currently not possible to accurately and non-invasively detect the location and persistence of the infused T cells. The goal of this work was to test cell sensitivity using ^{19}F MRI, which can later result in cell tracking in canines and eventually in humans.

To do this, canine T cells were expanded and then labeled with Cell Sense ^{19}F. First, peripheral blood was drawn from companion canines diagnosed with a malignancy. Using a Ficoll density gradient centrifugation, red blood cells were separated from the white blood cells. The T cells were then expanded on weekly additions of gamma-irradiated K562 cell line, which were genetically modified to express several T-cell specific co-stimulatory molecules. This cell line was also loaded with OKT3, a monoclonal antibody that binds to CD3 on the T cell, allowing expansion. The canine lymphoma cell line was in culture at 10^6 cells/mL in 20% FBS, 10 glutamax RPMI media with media changes occurring 2-3 times per week.

After a clinically sufficient number was obtained, the T cells or a canine lymphoma cell line was centrifuged and washed. The cells were re-suspended in *ex vivo* medium at a concentration between $3x10^6$ to $7x10^6$ cells/mL. Cell Sense ^{19}F was gently agitated and brought to room temperature. The cells were incubated in 5 mg/ml of ^{19}F for 18 hours at 38°C. Cells numbers and viability were determined before and after incubation using a Nexelcom Cellometer and trypan blue. Cells were then washed and resuspended in canine freeze media (10% DMSO, 40% canine plasma, 50% HBSS, filter sterilized 3 times) at various concentrations in 5 ml cryovials from Nalgene. The cells were frozen in -80°C freezer and shipped overnight to TIPS on dry ice for imaging.

VI.1 Cell Set #1

The first cell set used in this work was created on April 2, 2014 from a canine lymphoma cell line with a Cell Sense concentration of 5 mg/mL that contained $7x10^6$ cells/mL before incubation and $1x10^8$ cells/vial in a 5 mL vial after incubation. This vial was imaged using the spin echo and FLASH sequences.

The spin echo's parameters were TR of 1500 ms, TE of 15 ms, FOV of 500 mm, 5 mm slice thickness, matrix size of 128x128, voxel size of 3.9x3.9x5.0 mm^3, 5 averages, and TA of roughly 17 minutes. The vials with these parameters were scanned before the tests for the phantoms were done, therefore, they do not fit the ideal parameters requirements. However, they were used in this experiment because they resulted in a measurable signal that is at least 2.5 times stronger than the signal for the noise. Additionally, when multiple vials are compared with the same parameters, conclusions can still be made. The resulting ^{19}F MR image is shown in Fig 38.

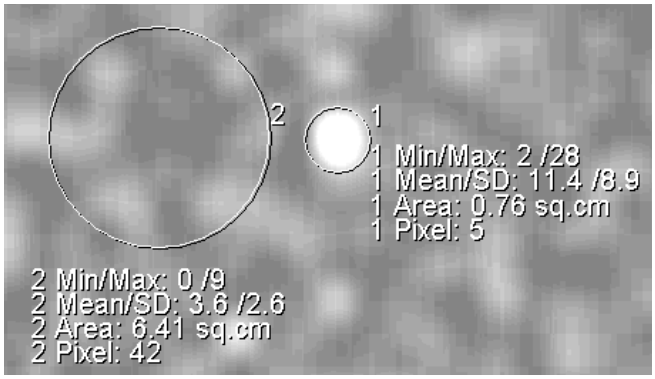

Figure 38: Spin echo ^{19}F MRI of cells containing 1E8 cells per vial. Parameters were TR of 1500 ms, TE of 15 ms, voxel size of 3.9x3.9x5.0 mm^3, and 5 averages.

Only one image, or slice, resulted in an identifiable signal because its intensity was considered significant compared to the intensity of the noise. Two ROIs were drawn, one around the signal of interest and the other around the noise or background signal. The signal intensity was calculated to be 11.4. In order to calculate the labeling efficiency, the equation calculated from the Cell Sense phantoms in Chapter VI was used. The term "labeling efficiency" was defined in this work as the amount of ^{19}F spins per cell. It should be noted that the number of ^{19}F spins can be directly related to the number of ^{19}F atoms, which is represented typically as spins/mm^3 (58). The signal intensity for the cells labeled with ^{19}F was calculated in Eq. 25 in order to find the estimated number of ^{19}F spins/mL.

$$\text{Signal Intensity} = 11.4 = (8\text{x}10^{-18})*(^{19}\text{F spins/mL}) + 9.2854 \qquad (25)$$

After solving this equation, the estimated ^{19}F concentration of this scan with a mean signal intensity of 11.4 was 2.64x10^{17} spins/mL. This 5 mL vial contained 2x10^7

cells/mL. The measured labeling efficiency of ^{19}F was calculated to be $1.32x10^{10}$ spins/cell.

This cell line was scanned using the FLASH sequence and resulted in 9 slices containing a signal with a significant intensity. These intensities were averaged for a value of 24.36. The parameters used were identical to the parameters used in the Cell Sense phantom experiment. These consisted of TR of 100 ms, TE of 5 ms, flip angle of 15°, FOV of 500 mm, 5 mm slice thickness, matrix size of 128x128, a voxel size of 3.9x3.9x5.0 mm^3, and 5 averages. Fig. 39 displayed one resulting image from the FLASH sequence. This was the same slice as the one used in the spin echo.

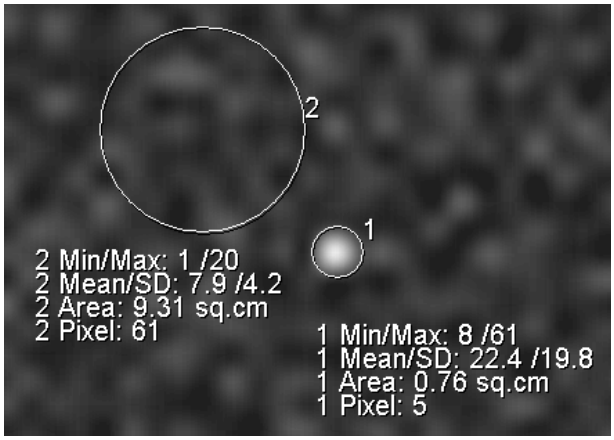

Figure 39: FLASH ^{19}F MRI of cells containing 1E8 cells per vial. Parameters were TR of 100 ms, TE of 5 ms, voxel size of 3.9x3.9x5.0 mm^3, and 5 averages.

The signal intensity was plugged into the Cell Sense phantom equation to solve for the measured labeling efficiency.

$$\text{Signal Intensity} = 24.63 = (6\text{x}10^{-17})*(^{19}\text{F spins/mL}) + 6.9601 \quad (26)$$

The resulting value was $2.94\text{x}10^{17}$ fluorine spins per mL. As before, this value was divided by the number of cells, which was $2\text{x}10^{7}$ cells/mL, to equal the detectable labeling efficiency of $1.47\text{x}10^{10}$ spins/cell. Using the FLASH sequence with the spin density defined parameters, a close but larger number of fluorine atoms per cell was detected as opposed to that of the spin echo sequence. Additional explanations and comparisons were given in the following cell set.

VI.2 Cell Set #2

The second cell set used in this work was created on April 2, 2014 from a canine lymphoma cell line with a Cell Sense concentration of 5 mg/mL that contained $7\text{x}10^{6}$ cells/mL before incubation and $2\text{x}10^{8}$ cells/vial in a 5 mL vial after incubation. The only difference between this cell set and the last was the increased cell count after incubation. This vial was imaged using the spin echo and FLASH sequences, and the quantification process of the previous cell set was repeated for this new cell set.

The spin echo's parameters were the same as the last set: TR of 1500 ms, TE of 15 ms, FOV of 500 mm, 5 mm slice thickness, matrix size of 128x128, voxel size of $3.9\text{x}3.9\text{x}5.0\ \text{mm}^3$, 5 averages, and TA of roughly 17 minutes. This scan resulted in one image where the signal was at least two and a half times greater than the noise (Fig. 40).

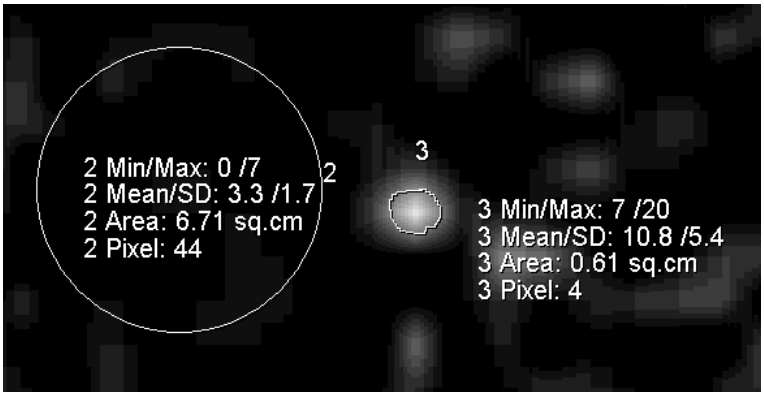

Figure 40: Spin echo ^{19}F MRI of cells containing 2E8 cells per vial. Parameters were TR of 1500 ms, TE of 15 ms, voxel size of 3.9x3.9x5.0 mm^3, and 5 averages.

The mean signal intensity was 10.8 and using the Eq. 27, the calculated number of fluorine spins was 1.89×10^{17} spins/mL.

$$\text{Signal Intensity} = 10.8 = (8 \times 10^{-18}) * (^{19}\text{F spins/mL}) + 9.2854 \qquad (27)$$

This value was divided by 4×10^7 cells/mL to get the measured labeling efficiency of 4.73×10^9 spins/cell.

The same vial was imaged using the FLASH sequence. The parameters were the same as the last cell set: TR of 100 ms, TE of 5 ms, flip angle of 15°, FOV of 500 mm, 5 mm slice thickness, matrix size of 128x128, a voxel size of 3.9x3.9x5.0 mm^3, and 5 averages. This sequence resulted in 10 slices where the signal mean intensity was significant compared to the noise. A slice example was shown in Fig. 41. These values were averaged to equal a signal intensity of 22.38. The signal intensity was plugged into Eq. 28 and resulted in 2.57×10^{17} fluorine spins/mL.

$$\text{Signal Intensity} = 22.38 = (6 \times 10^{-17}) * (^{19}\text{F spins/mL}) + 6.9601 \qquad (28)$$

The labeling efficiency was calculated by dividing $2.57x10^{17}$ fluorine spins/mL by $4x10^{7}$ cells/mL to get $6.43x10^{9}$ spins/cell.

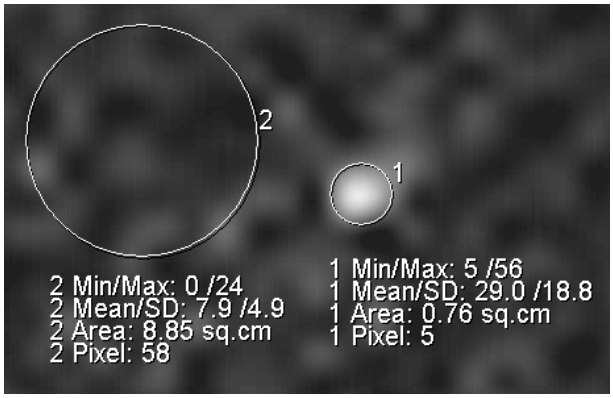

Figure 41: FLASH ^{19}F MRI of cells containing 2E8 cells per vial. Parameters were TR of 100 ms, TE of 5 ms, voxel size of 3.9x3.9x5.0 mm^3, and 5 averages.

This cell set using the FLASH sequence, as compared with the spin echo sequence, resulted in a largely higher number of fluorine spins. The results from the first and second cell set were compared in Table 3. In both cell sets, the FLASH sequence resulted in a larger number of measured ^{19}F spins/cell. Additionally, in the FLASH sequence, there were more slices with significant signal present. This may be ideal when doing *in vivo* studies because the detection amount has proven to be higher for the FLASH sequence.

Table 3: Results from Cell Set #1 and Cell Set #2 comparing the spin echo and FLASH sequences.

	Pulse Sequence	Slices with Signal Present	Mean Signal Intensity	Measured spins/mL	Measured spins/cell
Cell Set #1 $1x10^8$ cells/vial	SE	1	11.4	$2.64x10^{17}$	$1.32x10^{10}$
	FLASH	9	24.63	$2.94x10^{17}$	$1.47x10^{10}$
Cell Set #2 $2x10^8$ cells/vial	SE	1	10.8	$1.89x10^{17}$	$4.73x10^{9}$
	FLASH	10	22.38	$2.57x10^{17}$	$6.43x10^{9}$

It was also found that when increasing the cell count from $1x10^8$ cells/vial to $2x10^8$ cells/vial, the labeling efficiency was slightly lower. This could be possible because while keeping the fluorine concentration constant and increasing the cell count, each individual cell has a smaller amount of fluorine concentration inside. However, there is a limit to decreasing the number of cells and should be evaluated further. If too few fluorine labeled cells were injected in an animal, it is likely that ^{19}F MRI will fail. Unfortunately, the results comparing the relative mean intensity and number of cells/vial were not consistent with other works (59). This could be due to a number of reasons. The first being the manual methods used of drawing ROIs could be subjective. An automated method could prove to be more ideal and precise. Another explanation could be from the cell creation and incubation time period. A slight change in the way the cells were prepared slightly alter results. Additionally, the time period lapsed between scanning the vials could result in cell division, which could mean the assumption between the number of cells and the fluorine detected is now incorrect.

VI.3 Cell Set #3

The third cell set was created on May 8, 2014 from a canine lymphoma cell line with a Cell Sense concentration of 5 mg/mL that contained $7x10^6$ cells/mL before incubation and $1.0676x10^8$ cells/vial in a 5 mL vial after incubation. This vial was imaged using the spin echo and FLASH sequences with the ideal parameters and the parameters from the previous two cell sets.

First, the old parameters were evaluated for the spin echo which include TR of 1500 ms, TE of 15 ms, FOV of 500 mm, 5 mm slice thickness, matrix size of 128x128, voxel size of 3.9x3.9x5.0 mm^3, and 5 averages.

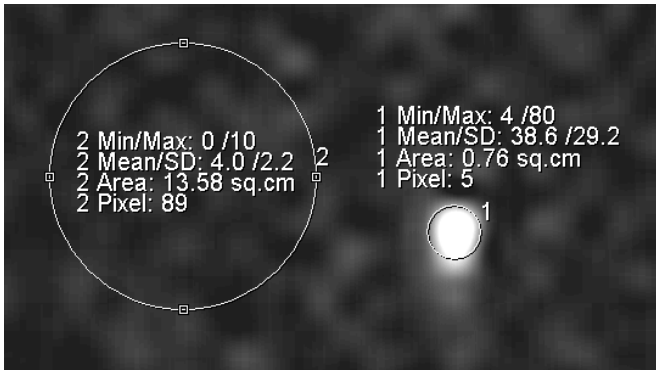

Figure 42: Spin echo ^{19}F MRI of cells containing 1.0676E8 cells per vial. Old parameters were used with TR of 1500 ms, TE of 15 ms, voxel size of 3.9x3.9x5.0 mm^3, and 5 averages.

This resulted in 5 slices with a mean intensity signal value of 15.04. One slice was shown in Fig. 42 for demonstration purposes. As before, ROIs were drawn around the signal area for each slice and averaged together to obtain the mean intensity signal value.

Using the same method as used for the previous cell sets, the mean intensity value for these sequence parameters resulted in 7.19×10^{17} spins/mL. This was divided by 2.14×10^{7} cells/mL to get the labeling efficiency of 3.69×10^{10} fluorine spins/cell.

The FLASH sequence was used with the old parameters for comparison. The parameters were the same as the last cell sets: TR of 100 ms, TE of 5 ms, flip angle of 15°, FOV of 500 mm, 5 mm slice thickness, matrix size of 128x128, a voxel size of 3.9x3.9x5.0 mm^3, and 5 averages. This sequence resulted in 10 slices with a mean signal intensity of 47.61. Fig. 43 represents a slice for the FLASH sequence in the same plane as the one in Fig. 42. As shown, the FLASH image compared to the spin echo image resulted more pixels with ^{19}F signal. Two ROIs were drawn around the present signals for comparison purposes. While the spin echo slice shown in Fig. 42 detected approximately 5 pixels, the FLASH sequence detected at least 39 pixels.

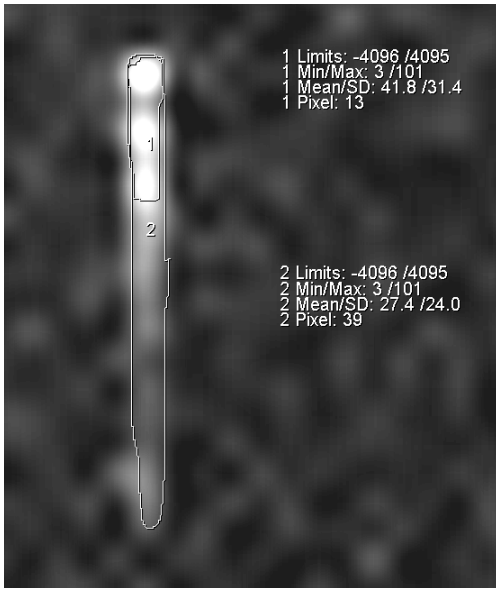

Figure 43: FLASH ^{19}F MRI of cells containing 1.0676E8 cells per vial. Parameters were TR of 100 ms, TE of 5 ms, voxel size of 3.9x3.9x5.0 mm^3, and 5 averages.

Using the same equation derived from the phantom study and used in the previous cell sets, a signal intensity of 47.61 resulted in 6.77x10^{17} spins/mL. Dividing this value by the total number of cells per mL resulted in a labeling efficiency of 3.17x10^{10} spins/cell.

The ideal parameters were used for this cell set for the spin echo sequence and consisted of spin density weighted image parameters (TR of 2000 ms and TE of 15 ms) with 32 averages, a matrix size of 64x64, and a large voxel size of 7.8x7.8x5.0 mm^3. Using these parameters for the 1.0676x10^8 cells/vial in a 5 mL vial resulted in 8 slices with significant signal with a mean signal intensity of 5.6. The equation showing the relationship between signal intensity and number of fluorine-19 spins per mL from the

Cell Sense phantoms in Chapter IV as shown in Eq. 29 was used for the labeling efficiency calculations.

$$\text{Signal Intensity} = (1\text{x}10^{-17})*(^{19}\text{F spins/mL}) + 0.1052 \quad (29)$$

A mean signal intensity of 5.6 resulted in $5.48\text{x}10^{17}$ spins/mL. This value was divided by the total number of cells per mL to obtain the measured labeling efficiency of $2.57\text{x}10^{10}$ fluorine-19 spins/cell. Fig. 44 represents a slice for the ideal parameters for the spin echo in the same plane as the previous two images.

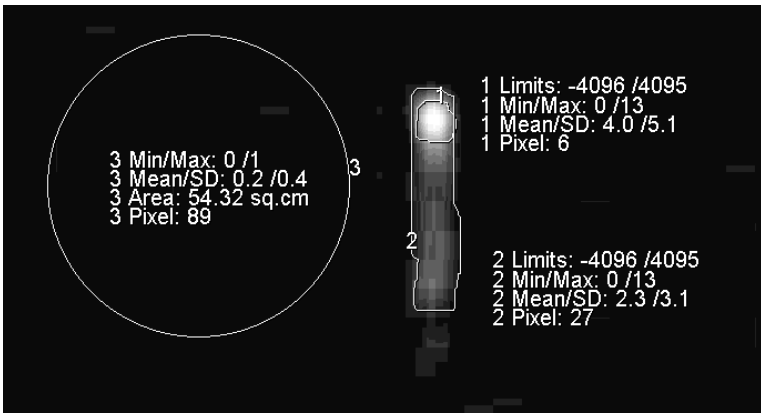

Figure 44: Spin echo ^{19}F MRI of cells containing 1.0676E8 cells per vial. Ideal parameters were used with TR of 2000 ms, TE of 15 ms, voxel size of 7.8x7.8x5.0 mm^3, and 32 averages.

The process was repeated for a final time using the ideal parameters for the FLASH sequence. These parameters include: TR of 100 ms, TE of 5 ms, 15° flip angle, a matrix size of 64x64, large voxel size of 7.8x7.8x5.0 mm^3, and 32 averages. This

resulted in every slice (21 total) with ^{19}F signal present. Fig. 45 shows one slice in the same plane as the previous scans.

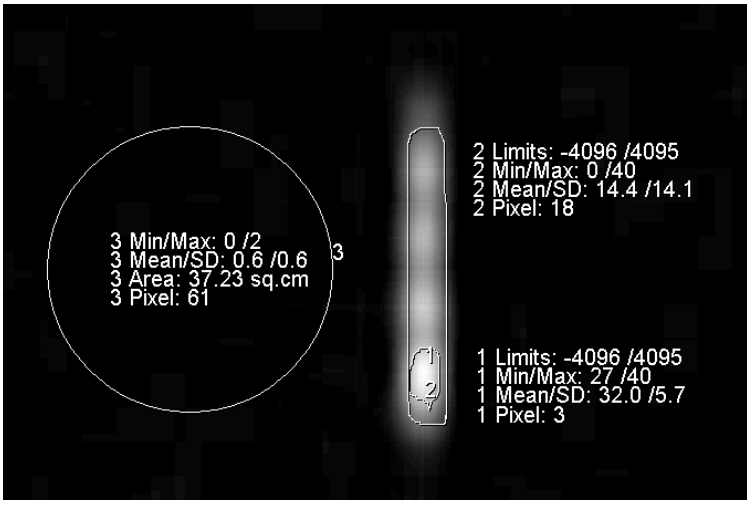

Figure 45: FLASH ^{19}F MRI of cells containing 1.0676E8 cells per vial. Ideal parameters were used with TR of 100 ms, TE of 5 ms, voxel size of 7.8x7.8x5.0 mm^3, and 32 averages.

The mean intensity signal for the 21 images was calculated to be 15.27. Using the equation derived from Chapter V for the Cell Sense phantoms, as shown in Eq. 30, the number of ^{19}F spins resulted in 4.40×10^{17} spins/mL.

$$\text{Signal Intensity} = (3 \times 10^{-17}) * (^{19}\text{F spins/mL}) + 2.0788 \qquad (30)$$

The measured labeling efficiency was calculated to be 2.06×10^{10} spins/cell.

Table 4 was created to compare the results from this cell set. The results showed that the old parameters resulted in a higher mean signal intensity, thus resulting in a

slightly higher measured labeling efficiency, as compared with the ideal parameters results. However, the ideal parameters resulted in roughly double the amount of slices with signal present. It was not only quantifiable but also more visibly detectable, as proven in the previous four figures. For example, Fig. 44, as compared with Fig. 42, displayed more pixels with present fluorine signal. The same occurs with the FLASH sequences for the old parameters image compared with the ideal parameters image. With this type of functional MR imaging with such small signal present, an increase in spatial resolution is not the goal. Instead, this cell set proves it will be of great importance to multinuclear studies to have a larger voxel size when the goal is to fuse the proton images with the multinuclear images. Fusing too few of pixels containing ^{19}F signal might not accurately show where the fluorine is present. Additionally, it is possible detection may not happen at all with the smaller voxel size.

Table 4: Results from Cell Set #3 with 1.0676E8 cells/vial

	Pulse Sequence	Slices with Signal Present	Mean Signal Intensity	Measured spins/mL	Measured spins/cell
Old Parameters	SE	5	15.04	7.19×10^{17}	3.69×10^{10}
	FLASH	10	47.61	6.77×10^{17}	3.17×10^{10}
Ideal Parameters	SE	8	5.6	5.48×10^{17}	2.57×10^{10}
	FLASH	21	15.27	4.40×10^{17}	2.06×10^{10}

The results for the ideal parameters also resulted in the spin echo detecting a slightly higher amount of fluorine per cell. These results seem to be the opposite case of what happened in the previous two cell sets. One possible explanation for this could be the ROI manual drawing method. For example, because there were so few pixels with signal present, the absence of one pixel in the ROI may drastically alter the mean signal intensity. This human error would be minimized if there were a more automatic method for these calculations. Another factor that could affect these calculations is cell division. It would be ideal if the amount of 19F per cell was constant but it has been shown that it will decrease by half with each cell division (43). The amount of time after cell transfer might have varied slightly, therefore, that will affect the MRI cell quantification. The actual division rate of these T cells was unknown and may contribute to a somewhat imprecise cell quantification.

CHAPTER VII

CONCLUSIONS AND FUTURE WORK

The objective of this work was to enable and test multinuclear MRI, specifically for fluorine-19, on a Siemens Verio. To do so, a spin echo sequence and a type of spoiled gradient echo sequence, which Siemens named FLASH, were evaluated and implemented to resonate at the fluorine frequency, instead of the typical hydrogen resonant frequency. The sequences were tested virtually for RF pulse, gradient, and ADC timings, programming errors, and parameter limits. The C++ files and libraries were then compiled and transferred to the Siemens Verio. The sequences were tested on fluorine-19 phantoms in order to find the ideal parameters for ^{19}F MRI. Additionally, the sequences were tested *ex vivo*. Canine lymphoma cells were labeled with fluorine-19 and imaged to conclude its detection capabilities.

The FLASH sequence resulted in a larger number of slices with signal present. This may be a beneficial quality in future animal studies. Additionally, the labeling efficiency resulted in maximum of 3.69×10^{10} spins/cell. Celsense proved the detection limit for T cells for 5.0 mg/mL of 19F to be approximately 4×10^{11} spins/cell (60). However, this was at 7T, so detection will be slightly lower for 3T. Therefore, the maximum labeling efficiency calculated in the cell set experiments proved to be a good estimation for ^{19}F labeled T cells at MRI strength of 3T.

Future work will be implementing one, or both, of these sequences for *in vivo* studies. Hydrogen MR images will be taken to obtain an anatomical view of the animal.

Using the same slice thickness and FOV dimensions, ^{19}F MR images will be taken to track the fluorine labeled cells within the body. These images can be fused together to result in the specific location of the fluorine (61). Using the results from the cell sets evaluated in this work, cell quantification can analyzed to determine the number of labeled cells present in each voxel and the total number of cells needed for signal detection. Additionally, Celsense has developed software, called Voxel Tracker, capable of tracking and quantifying ^{19}F labeled cells. Unfortunately, these two methods involve manually drawing ROIs and are susceptible to human error. An automated method would potentially be more precise and consistent for cell quantification.

Another future addition to this study would be to broaden the scope of the multinuclear pulse sequences available at TIPS. Some previous studies have shown success with fast/turbo spin echo sequences (FSE/TSE) and rapid acquisition with relaxation enhancement (RARE) sequences for ^{19}F MRI in improving sensitivity threshold and SNR (62-65). Chemical shift imaging (CSI) and spectroscopy have been examined by many in which the molecule of choice contains different atoms that exhibit multiple resonating frequencies (66-70). Although this was not found to be a major problem in this work due to the PFC used, others have noted the usefulness of such sequences (71).

Overall, the major contributions of this work reside in testing a method for imaging and tracking fluorine-19 labeled cells using the Siemens 3T Verio MR scanner located at TIPS. Using this method, researchers involved in cellular therapy will be able to accurately and non-invasively track infused cells. The positive ^{19}F signal will prove

to be advantageous for tracking areas such as lungs, liver, and bone where other methods like metal ion based contrast agents are limited by the low signal areas with strong background contrast. Also, it was proven that the ^{19}F labeled cells could be quantified, in addition to tracking. This quantitative analysis will aid researchers in determining and analyzing the efficiency of cellular therapy.

REFERENCES

1. Brittberg M, Lindahl A, Nilsson A, Ohlsson C, Isaksson O, Peterson L. Treatment of deep cartilage defects in the knee with autologous chondrocyte transplantation. New England Journal of Medicine 1994;331(14):889-895.

2. Peterson L, Minas T, Brittberg M, Nilsson A, Sjögren-Jansson E, Lindahl A. Two-to 9-year outcome after autologous chondrocyte transplantation of the knee. Clinical Orthopaedics and Related Research 2000;374:212-234.

3. Björklund A, Lindvall O. Cell replacement therapies for central nervous system disorders. Nature Neuroscience 2000;3(6).

4. Ashley DM, Faiola B, Nair S, Hale LP, Bigner DD, Gilboa E. Bone marrow–generated dendritic cells pulsed with tumor extracts or tumor RNA induce antitumor immunity against central nervous system tumors. The Journal of Experimental Medicine 1997;186(7):1177-1182.

5. Gilboa E, Nair SK, Lyerly HK. Immunotherapy of cancer with dendritic-cell-based vaccines. Cancer Immunology, Immunotherapy 1998;46(2):82-87.

6. Boss WK, Usal H, Chernoff G, Keller GS, Lask GP, Fodor PB. Autologous cultured fibroblasts as cellular therapy in plastic surgery. Clinics in Plastic Surgery 2000;27(4):613-626.

7. Yee C, Thompson J, Byrd D, Riddell S, Roche P, Celis E, Greenberg P. Adoptive T cell therapy using antigen-specific CD8+ T cell clones for the treatment of patients with metastatic melanoma: in vivo persistence, migration, and antitumor effect of transferred T cells. Proceedings of the National Academy of Sciences 2002;99(25):16168-16173.

8. Peggs KS, Verfuerth S, Pizzey A, Khan N, Guiver M, Moss PA, Mackinnon S. Adoptive cellular therapy for early cytomegalovirus infection after allogeneic stem-cell transplantation with virus-specific T-cell lines. The Lancet 2003;362(9393):1375-1377.

9. Rajnoch C, Chachques J-C, Berrebi A, Bruneval P, Benoit M-O, Carpentier A. Cellular therapy reverses myocardial dysfunction. The Journal of Thoracic and Cardiovascular Surgery 2001;121(5):871-878.

10. Costa GL, Sandora MR, Nakajima A, Nguyen EV, Taylor-Edwards C, Slavin AJ, Contag CH, Fathman CG, Benson JM. Adoptive immunotherapy of experimental

autoimmune encephalomyelitis via T cell delivery of the IL-12 p40 subunit. The Journal of Immunology 2001;167(4):2379-2387.

11. Yang M, Baranov E, Jiang P, Sun F-X, Li X-M, Li L, Hasegawa S, Bouvet M, Al-Tuwaijri M, Chishima T. Whole-body optical imaging of green fluorescent protein-expressing tumors and metastases. Proceedings of the National Academy of Sciences 2000;97(3):1206-1211.

12. Stodilka RZ, Blackwood KJ, Prato FS. Tracking transplanted cells using dual-radionuclide SPECT. Physics in Medicine and Biology 2006;51(10):2619.

13. Phelps ME. Molecular imaging with positron emission tomography. Annual Review of Nuclear and Particle Science 2002;52(1):303-338.

14. Lauterbur PC. Image formation by induced local interactions: examples employing nuclear magnetic resonance. Nature 1973;242(5394):190-191.

15. Henning TD, Saborowski O, Golovko D, Boddington S, Bauer JS, Fu Y, Meier R, Pietsch H, Sennino B, McDonald DM. Cell labeling with the positive MR contrast agent Gadofluorine M. European Radiology 2007;17(5):1226-1234.

16. Giesel FL, Stroick M, Griebe M, Tröster H, Claus W, Requardt M, Rius M, Essig M, Kauczor H-U, Hennerici MG. Gadofluorine m uptake in stem cells as a new magnetic resonance imaging tracking method: an in vitro and in vivo study. Investigative Radiology 2006;41(12):868-873.

17. de Vries IJM, Lesterhuis WJ, Barentsz JO, Verdijk P, van Krieken JH, Boerman OC, Oyen WJ, Bonenkamp JJ, Boezeman JB, Adema GJ. Magnetic resonance tracking of dendritic cells in melanoma patients for monitoring of cellular therapy. Nature Biotechnology 2005;23(11):1407-1413.

18. Bulte JW, Kraitchman DL. Iron oxide MR contrast agents for molecular and cellular imaging. NMR in Biomedicine 2004;17(7):484-499.

19. Yeh TC, Zhang W, Ildstad ST, Ho C. Intracellular labeling of T-cells with superparamagnetic contrast agents. Magnetic Resonance in Medicine 1993;30(5):617-625.

20. Ahrens ET, Flores R, Xu H, Morel PA. In vivo imaging platform for tracking immunotherapeutic cells. Nature Biotechnology 2005;23(8):983-987.

21. Partlow KC, Chen J, Brant JA, Neubauer AM, Meyerrose TE, Creer MH, Nolta JA, Caruthers SD, Lanza GM, Wickline SA. 19F magnetic resonance imaging for

stem/progenitor cell tracking with multiple unique perfluorocarbon nanobeacons. The FASEB Journal 2007;21(8):1647-1654.

22. Flögel U, Ding Z, Hardung H, Jander S, Reichmann G, Jacoby C, Schubert R, Schrader J. In vivo monitoring of inflammation after cardiac and cerebral ischemia by fluorine magnetic resonance imaging. Circulation 2008;118(2):140-148.

23. Janjic JM, Ahrens ET. Fluorine-containing nanoemulsions for MRI cell tracking. Wiley Interdisciplinary Reviews: Nanomedicine and Nanobiotechnology 2009;1(5):492-501.

24. Purcell EM, Torrey H, Pound RV. Resonance absorption by nuclear magnetic moments in a solid. Physical Review 1946;69(1-2):37.

25. Bloch F. Nuclear induction. Physical Review 1946;70(7-8):460.

26. Prince JL, Links JM. Medical imaging signals and systems: Pearson Prentice Hall Upper Saddle River, NJ; 2006.

27. Elst LV, Maton F, Laurent S, Seghi F, Chapelle F, Muller RN. A multinuclear MR study of Gd-EOB-DTPA: Comprehensive preclinical characterization of an organ specific MRI contrast agent. Magnetic Resonance in Medicine 1997;38(4):604-614.

28. Samee S, Altes T, Powers P, de Lange EE, Knight-Scott J, Rakes G, Mugler III JP, Ciambotti JM, Alford BA, Brookeman JR. Imaging the lungs in asthmatic patients by using hyperpolarized helium-3 magnetic resonance: assessment of response to methacholine and exercise challenge. Journal of Allergy and Clinical Immunology 2003;111(6):1205-1211.

29. Kushnir T, Itzchak Y, Valevski A, Lask M, Modai I, Navon G. Relaxation times and concentrations of 7Li in the brain of patients receiving lithium therapy. NMR in Biomedicine 1993;6(1):39-42.

30. Hu S, Chen AP, Zierhut ML, Bok R, Yen Y-F, Schroeder MA, Hurd RE, Nelson SJ, Kurhanewicz J, Vigneron DB. In vivo carbon-13 dynamic MRS and MRSI of normal and fasted rat liver with hyperpolarized 13C-pyruvate. Molecular Imaging and Biology 2009;11(6):399-407.

31. Reddy R, Insko EK, Noyszewski EA, Dandora R, Kneeland JB, Leigh JS. Sodium MRI of human articular cartilage in vivo. Magnetic Resonance in Medicine 1998;39(5):697-701.

32. Moseley M, Cohen Y, Mintorovitch J, Chileuitt L, Shimizu H, Kucharczyk J, Wendland M, Weinstein P. Early detection of regional cerebral ischemia in cats: comparison of diffusion-and T2-weighted MRI and spectroscopy. Magnetic Resonance in Medicine 1990;14(2):330-346.

33. Duhamel G, Choquet P, Grillon E, Lamalle L, Leviel JL, Ziegler A, Constantinesco A. Xenon-129 MR imaging and spectroscopy of rat brain using arterial delivery of hyperpolarized xenon in a lipid emulsion. Magnetic Resonance in Medicine 2001;46(2):208-212.

34. Ruiz-Cabello J, Barnett BP, Bottomley PA, Bulte JW. Fluorine (19F) MRS and MRI in biomedicine. NMR in Biomedicine 2011;24(2):114-129.

35. Bosselmann S, Owens III DE, Kennedy RL, Herpin MJ, Williams III RO. Plasma deposited stability enhancement coating for amorphous ketoprofen. European Journal of Pharmaceutics and Biopharmaceutics 2011;78(1):67-74.

36. Clark LC, Gollan F. Survival of mammals breathing organic liquids equilibrated with oxygen at atmospheric pressure. Science 1966;152(3730):1755-1756.

37. Haselgrove J, Prammer M. An algorithm for compensation of surface-coil images for sensitivity of the surface coil. Magnetic Resonance Imaging 1986;4(6):469-472.

38. Kneeland JB, Hyde JS. High-resolution MR imaging with local coils. Radiology 1989;171(1):1-7.

39. Rojas R, Rodriguez AO. Numerical study of the SNR and SAR of MRI coil arrays. In: 29th Annual International Conference of the IEEE. Lyon, France, 2007. p 1196-1199.

40. Haase A, Odoj F, Von Kienlin M, Warnking J, Fidler F, Weisser A, Nittka M, Rommel E, Lanz T, Kalusche B. NMR probeheads for in vivo applications. Concepts in Magnetic Resonance 2000;12(6):361-388.

41. Schneider G, Martin D, Grazioli L, Olivetti L, Saini S, Luca A, Kirchin M, Massmann A, Seidel R, Romanini L. MRI of the liver: imaging techniques, contrast enhancement, differential diagnosis: Springer; 2006.

42. Constantinides CD, Atalar E, McVeigh ER. Signal-to-noise measurements in magnitude images from NMR phased arrays. Magnetic Resonance in Medicine 1997;38(5):852-857.

43. Srinivas M, Morel PA, Ernst LA, Laidlaw DH, Ahrens ET. Fluorine-19 MRI for visualization and quantification of cell migration in a diabetes model. Magnetic Resonance in Medicine 2007;58(4):725-734.

44. Gudbjartsson H, Patz S. The Rician distribution of noisy MRI data. Magnetic Resonance in Medicine 1995;34(6):910-914.

45. Caruthers SD, Neubauer AM, Hockett FD, Lamerichs R, Winter PM, Scott MJ, Gaffney PJ, Wickline SA, Lanza GM. In vitro demonstration using 19F magnetic resonance to augment molecular imaging with paramagnetic perfluorocarbon nanoparticles at 1.5 Tesla. Investigative Radiology 2006;41(3):305-312.

46. Haase A, Frahm J, Matthaei D, Hanicke W, Merboldt K-D. FLASH imaging. Rapid NMR imaging using low flip-angle pulses. Journal of Magnetic Resonance (1969) 1986;67(2):258-266.

47. Bernstein MA, King KF, Zhou XJ. Handbook of MRI pulse sequences: Elsevier; 2004.

48. Wood ML, Silver M, Runge VM. Optimization of spoiler gradients in FLASH MRI. Magnetic Resonance Imaging 1987;5(6):455-463.

49. Crawley AP, Wood ML, Henkelman RM. Elimination of transverse coherences in FLASH MRI. Magnetic Resonance in Medicine 1988;8(3):248-260.

50. Weber H, Purdy D, Deimling M, Oppelt A. Contrast behaviour of the fast imaging sequences FLASH and FISP: results from synthetic images. Society of Magnetic Resonance in Medicine (SMRM) 1986:957-958.

51. O'Connor CM, Sheppard S, Hartline CA, Huls H, Johnson M, Palla SL, Maiti S, Ma W, Davis RE, Craig S. Adoptive T-cell therapy improves treatment of canine non–Hodgkin lymphoma post chemotherapy. Scientific Reports 2012;2.

52. Paoloni M, Khanna C. Translation of new cancer treatments from pet dogs to humans. Nature Reviews Cancer 2008;8(2):147-156.

53. Paoloni MC, Khanna C. Comparative oncology today. Veterinary Clinics of North America: Small Animal Practice 2007;37(6):1023-1032.

54. Dupont J, Latouche J-B, Ma C, Sadelain M. Artificial Antigen-Presenting Cells Transduced with Telomerase Efficiently Expand Epitope-Specific, Human Leukocyte Antigen–Restricted Cytotoxic T Cells. Cancer Research 2005;65(12):5417-5427.

55. Maus MV, Thomas AK, Leonard DG, Allman D, Addya K, Schlienger K, Riley JL, June CH. Ex vivo expansion of polyclonal and antigen-specific cytotoxic T lymphocytes by artificial APCs expressing ligands for the T-cell receptor, CD28 and 4-1BB. Nature Biotechnology 2002;20(2):143-148.

56. Suhoski MM, Golovina TN, Aqui NA, Tai VC, Varela-Rohena A, Milone MC, Carroll RG, Riley JL, June CH. Engineering artificial antigen-presenting cells to express a diverse array of co-stimulatory molecules. Molecular Therapy 2007;15(5):981-988.

57. Singh H, Manuri PR, Olivares S, Dara N, Dawson MJ, Huls H, Hackett PB, Kohn DB, Shpall EJ, Champlin RE. Redirecting specificity of T-cell populations for CD19 using the Sleeping Beauty system. Cancer Research 2008;68(8):2961-2971.

58. Balducci A, Helfer BM, Ahrens ET, O'Hanlon CF, Wesa AK. Visualizing arthritic inflammation and therapeutic response by fluorine-19 magnetic resonance imaging (19F MRI). J Inflammation (London, UK) 2012;9(1):24-34.

59. Bible E, Dell'Acqua F, Solanky B, Balducci A, Crapo PM, Badylak SF, Ahrens ET, Modo M. Non-invasive imaging of transplanted human neural stem cells and ECM scaffold remodeling in the stroke-damaged rat brain by 19F and diffusion-MRI. Biomaterials 2012;33(10):2858-2871.

60. Helfer BM, Balducci A, Nelson AD, Janjic JM, Gil RR, Kalinski P, De Vries IJM, Ahrens ET, Mailliard RB. Functional assessment of human dendritic cells labeled for in vivo 19F magnetic resonance imaging cell tracking. Cytotherapy 2010;12(2):238-250.

61. Flögel U, Su S, Kreideweiss I, Ding Z, Galbarz L, Fu J, Jacoby C, Witzke O, Schrader J. Noninvasive detection of graft rejection by in vivo 19F MRI in the early stage. American Journal of Transplantation 2011;11(2):235-244.

62. Mastropietro A, Bernardi E, Breschi GL, Zucca I, Cametti M, Soffientini CD, Curtis M, Terraneo G, Metrangolo P, Spreafico R. Optimization of rapid acquisition with relaxation enhancement (RARE) pulse sequence parameters for 19F-MRI studies. Journal of Magnetic Resonance Imaging 2013;40(1):162-170.

63. Ohno Y, Hatabu H. Basics concepts and clinical applications of oxygen-enhanced MR imaging. European Journal of Radiology 2007;64(3):320-328.

64. Higuchi M, Iwata N, Matsuba Y, Sato K, Sasamoto K, Saido TC. 19F and 1H MRI detection of amyloid β plaques in vivo. Nature Neuroscience 2005;8(4):527-533.

65. Schmid F, Hoeltke C, Parker D, Faber C. Boosting 19F MRI—SNR efficient detection of paramagnetic contrast agents using ultrafast sequences. Magnetic Resonance in Medicine 2013;69(4):1056-1062.

66. Hertlein T, Sturm V, Kircher S, Basse-Lüsebrink T, Haddad D, Ohlsen K, Jakob P. Visualization of abscess formation in a murine thigh infection model of Staphylococcus aureus by 19F-magnetic resonance imaging (MRI). PloS One 2011;6(3):e18246.

67. Weise G, Basse-Lüsebrink TC, Kleinschnitz C, Kampf T, Jakob PM, Stoll G. In vivo imaging of stepwise vessel occlusion in cerebral photothrombosis of mice by 19F MRI. PloS One 2011;6(12):e28143.

68. Sassa T, Suhara T, Ikehira H, Obata T, Girard F, Tanada S, Okubo Y. 19F-magnetic resonance spectroscopy and chemical shift imaging for schizophrenic patients using haloperidol decanoate. Psychiatry and Clinical Neurosciences 2002;56(6):637-642.

69. Venkatasubramanian PN, Shen YJ, Wyrwicz AM. Characterization of the cerebral distribution of general anesthetics in vivo by two-dimensional 19F chemical shift imaging. Magnetic Resonance in Medicine 1996;35(4):626-630.

70. Kok MB, de Vries A, Abdurrachim D, Prompers JJ, Grüll H, Nicolay K, Strijkers GJ. Quantitative 1H MRI, 19F MRI, and 19F MRS of cell-internalized perfluorocarbon paramagnetic nanoparticles. Contrast Media & Molecular Imaging 2011;6(1):19-27.

71. Janjic JM, Srinivas M, Kadayakkara DK, Ahrens ET. Self-delivering nanoemulsions for dual fluorine-19 MRI and fluorescence detection. Journal of the American Chemical Society 2008;130(9):2832-2841.